The multichannel motional Stark effect diagnostic in the JFT-2M tokamak

Kensaku Kamiya

DOCTOR OF PHILOSOPHY

Department of Fusion Science

School of Mathematical and Physical Science

The Graduate University for Advanced Studies

2000

Abstract

The q-profile plays a key role in determining the equilibrium, stability, and transport of plasma in toroidal magnetic confinement configurations, where q denotes the inverse of the rotational transform of the magnetic field line. Accurate determination of the q-profile is thus essential for a quantitative analysis. Experimental techniques to improve the confinement and sustain it for a long pulse by active control of the q-profile, using radiofrequency (RF) wave, neutral beams, or bootstrap current, have been tested in tokamaks. Progress in these studies has largely been due to development of diagnostic techniques such as motional Stark effect (MSE) to measure the q-profile reliably.

A multichannel motional Stark effect polarimeter system, which is capable of simultaneous measurement of a radial electric field, has recently been installed on JFT-2M. The diagnostic can measure the polarization angle at 18 radial location, which cover a region between just inside from the magnetic axis and the outboard edge of the plasma. After careful calibration of the instrument, the magnetic field pitch angle [$\gamma_p=\tan^{-1}(B_P/B_T)$] is obtained with a statistical uncertainty of about 0.1° with a time resolution of 10 ms. In order to determine the equilibrium selfconsistently, the free boundary equilibrium code (CUPID; CUrrent Profile IDentification code) has also been introduced on JFT-2M, which solves the Grad-Shafranov equation using internal magnetic field data measured by MSE in conjunction with external magnetic data measured by magnetic probes, flux loops, and Rogowski coils at several locations outside the plasma.

In L-mode discharges with different plasma current I_p and its ramp up rates

dI_P/dt, it is found that sawtooth crashes emerges reproductively just after the q(0) pass through ~ unity, and it occurs at earlier time-slice as the discharges of larger I_P (and smaller surface q values) at the flat top, irrespective of the dI_P/dt. After sawtooth crash, the q(0) keeps constant value of below ~ unity throughout the sawtooth cycle as observed in many tokamaks. As the result of the equilibrium reconstruction by CUPID code, it is confirmed that plasma currents are ramped up with a broad profile (with a monotonic q-profile), and it is also observed a significant peaking of the current profile with the peaking of the soft X-ray emission in the plasma core, but sawtooth crash appears nothing yet showing $q(0) > 1$.

Outstanding feature of the MSE system on JFT-2M is that it makes possible to separate the effect of the radial electric field (E_r) from the polarization angle measurements. By viewing two neural beam lines (one is co-parallel to the plasma current and the other is counter-parallel) simultaneously and near tangentially to the toroidal magnetic field from only one spectroscopic instruments, it provides the best sensitivity in E_r measurements with good spatial resolution. The magnetic field pitch angle is also measured with a smallest uncertainty. Such a method of E_r measurement with MSE using two beam lines, which is the first attempt in the world, can provide the best accuracy among other techniques. Preliminary data of δE_r (the change in the radial electric field) profile in L-mode plasma has been obtained. Comparison with calculated δE_r profile using CXRS measurements of the toroidal rotation velocity will also discussed.

Acknowledgements

The author wishes to acknowledge the support of the many people at Japan Atomic Energy Research Institute (JAERI) and National Institute for fusion Science (NIFS) who made the diagnostic possible. A special thanks goes to Drs. T. Fujita, H. Kimura and Y. Miura of JAERI and Prof. Y. Hamada and Dr. K. Ida of NIFS for their generous support to this study in terms of advice, discussion and unpublished work. Also Dr. M. Azumi of JAERI for his programming work on the equilibrium code and the JFT-2M group for their capable operation.

Contents

Chapter 1

Introduction

1.1 Overview

The controlled thermonuclear fusion is one of candidate method providing energy in future. It has environmental advantages such as no carbon emissions and low radioactivity in addition to the abundant fuel of deuterium and lithium that are available to all nations. Progress in both experimental and theoretical techniques for the improvement of plasma confinement in the last few years has made it possible to create the plasma with the temperature of ~ 10 keV reproductively. Enhanced core confinement or the formation of an internal transport barrier (ITB) has been demonstrated in reversed magnetic shear [= 2V/q(dq/dV) where q is the inverse of the rotational transform of the magnetic field lines (safety factor) and V is the flux surface volume] discharge in many tokamaks [1-5]. In these discharges, however, improved performance is limited by magnetohydrodynamic (MHD) stability at high β, and it has also many problems which cannot be solved yet, such as impurity accumulation, He ash exhaust, and its long time sustainment. One technique to improve the MHD stability of these operation consistent with improved performance is to control the current density profile using NB and RF [6], which also provide a technique of noninductive current drive for long time sustainment. Measuring the current density profile is thus essential for quantitative analysis of MHD stability and confinement of the tokamak plasma.

It is well known that external magnetic measurements alone only yield the plasma shape and global current profile parameters such as β_p and l_i in tokamak [7, 8]. If internal magnetic and/or kinetic data are combined self-consistency with external magnetic data, it can improve the accuracy of the MHD equilibrium reconstruction and determine the detail structure of profiles of the current density and the safety factor. The recent development of motional Stark effect polarimetry measurements of the localized and internal poloidal magnetic field provide a better constraint for the equilibrium, since it has advantage in spatial resolution compared with other non-localized measurements such as Faraday rotation measurement [9-12].

In this study, a multichannnel motional Stark effect diagnostic system has been installed on JFT-2M. By viewing two neural beam lines (one is co-parallel to the plasma current and the other is counter-parallel) simultaneously and near tangentially to the toroidal magnetic field from only one spectroscopic instruments, it provides the best sensitivity in radial electric field (E_r) measurements with good spatial resolution. The magnetic field pitch angle is also measured with the smallest uncertainty. In order to determine the equilibrium selfconsistently, the free boundary equilibrium code (CUPID; CUrrent Profile IDentification code) has also been introduced on JFT-2M, which solves the Grad-Shafranov equation using internal magnetic field data measured by MSE in conjunction with external magnetic data measured by magnetic probes, flux loops, and Rogowski coils at several locations outside the plasma. The time behaviors of profiles of the current density and the safety factor are investigated for several plasma conditions including L-mode discharge with sawtooth activity and current ramp. The E_r profile measurement is also performed in L-mode plasma where opposite neutral beam torque is applied.

1.2 Principle of motional Stark effect polarimetry

The motional Stark effect (MSE) diagnostic is well-established technique for internal magnetic field measurements, and it is now used on many tokamaks [9-12]. This diagnostic can measure the direction of the polarization of line emission from hydrogen or deuterium atom in a heating or diagnostic neutral beam. The emission from Balmer-alpha transition, n=3→2 (H_α or D_α), is excited from the n=1 state due to the collision between the neutral beam and the electron in the plasma. The energy level, E_n in cm^{-1}, with the electric field, E in V/cm, is given by

$$E_n = -\frac{1.097\times10^5}{n^2} + \frac{E}{15620}n(n_1 - n_2), \tag{1-2-1}$$

where n is the principal quantum number. The first term represents the energy level without electric field, while the second one represents the splitting of energy levels due to the Stark effect. The n=2 energy level splits into three, while the n=3 energy level splits into five as shown in Fig. 1.2.1. As a neutral beam with high velocity ($\mathbf{v_b}$) across the magnetic field ($\mathbf{B}$), the Lorentz electric field ($\mathbf{E_L} = \mathbf{v_b}\times\mathbf{B}$) is induced in the atom's rest frame.

The Stark effect produces splitting of the Balmer-alpha line into 15 components, only nine of which have appreciable intensity. The wavelength splitting between adjacent components is given by

$$\Delta\lambda_{Stark}=2.7574\times10^{-7}\,E, \tag{1-2-2}$$

where E is the electric field strength (in V/m), and $\Delta\lambda$ is in Å. Fig. 1.2.2 shows simulation of full energy Stark spectrum for an 32 keV hydrogen beam and profile of 3 Å FWHM filter, which is usually used in almost all tokamaks. Magnetic field 2 T, beam

velocity component perpendicular to the magnetic field 2.5×10^6 m/s (electric field 3.5×10^6 V/m). As shown in Fig. 1.2.3, the net polarization fraction [$P_f^{net}=(I_\sigma-I_\pi)/(I_\sigma+I_\pi)$ x(filter profile)] is estimated to be about 50 % in this condition. The measurements of the pitch angle were done in the JFT-2M tokamak, at a magnetic field of 0.8 ~ 2.2 T and a beam energy of 32 keV, which are typical operating parameters on JFT-2M. The average spectral shift of the π lines due to the Stark effect for this field is about 2 ~ 4 Å and the signal to noize ratio (S/N) must be poor on the condition of low magnetic field such as ~ 1T.

When viewed in a direction perpendicular to $\mathbf{E}_L$, the Stark split σ and π components are polarized respectively perpendicular and parallel to the direction of $\mathbf{E}_L$. When viewed along $\mathbf{E}_L$ the σ components are unpolarized and the π components have no intensity. In general, if the viewing sightline and neutral beam line are in near midplane of the device as shown in Fig. 1.2.4, the relation between the magnetic field pitch angle (γ_p) and measured polarization angle (γ_m) is given by

$$\tan \gamma_m = v_b B_Z \cos(\alpha+\Omega) / v_b B_T \sin(\alpha) \equiv C(\alpha, \Omega) \tan(\gamma_p) , \qquad (1\text{-}2\text{-}3)$$

where B_Z is the vertical magnetic field, B_T is toroidal magnetic field, α is the angle between the viewing sight line and neutral beam line, Ω is the angle between the viewing sight line and the toroidal magnetic field line, and $C(\alpha, \Omega)$ is geometrical constant. Thus, the pitch angle measurement takes advantage of the fact that the direction of linear polarization of Stark components is directly related to the direction of the local magnetic field.

The line emissions from high-energy hydrogen or deuterium beam have a number of features which allow the motional Stark effect diagnostic to achieve a highly accurate measurement of the polarization angle [13]:

(i) For the typical tokamak and neutral beam parameters (for example, the toroidal magnetic field of $B_T > 1$ T and the accelerated voltage of the hydrogen beam ion of $V_{acc}^{H+} > 30$ kV), the Stark effect splitting is of the order of the spectral line width and thus a large fractional polarization of the line is observed.

(ii) Hydrogen or deuterium have the unique characteristic that the Stark effect is linear with respect to the electric field, producing a large spectral shift, much larger than the Zeeman shift ($\delta\lambda_z = 4.67 \times 10^{-9} \lambda_0^2 B \sim 0.4$ Å for $B = 2$ T and $\lambda_0 =$ 6563 Å) which can be ignored at these beam energies.

(iii) With proper observation geometry, Doppler shifted emissions may be employed and the analyzed radiation may be spectrally separated from the strong thermal background of H_α and/or D_α emissions (at 6563 Å) and impurity lines such as CII (at 6578 Å and 6583 Å).

(iv) The sample volume is localized to the intersection of the sightline and the neutral beam line.

(v) In general, the high-energy neutral beam penetrates far enough into the plasma to provide strong emission from the plasma interior.

(vi) The analyzed beam emissions are in the visible range of wavelength for which the polarizating optics is readily available.

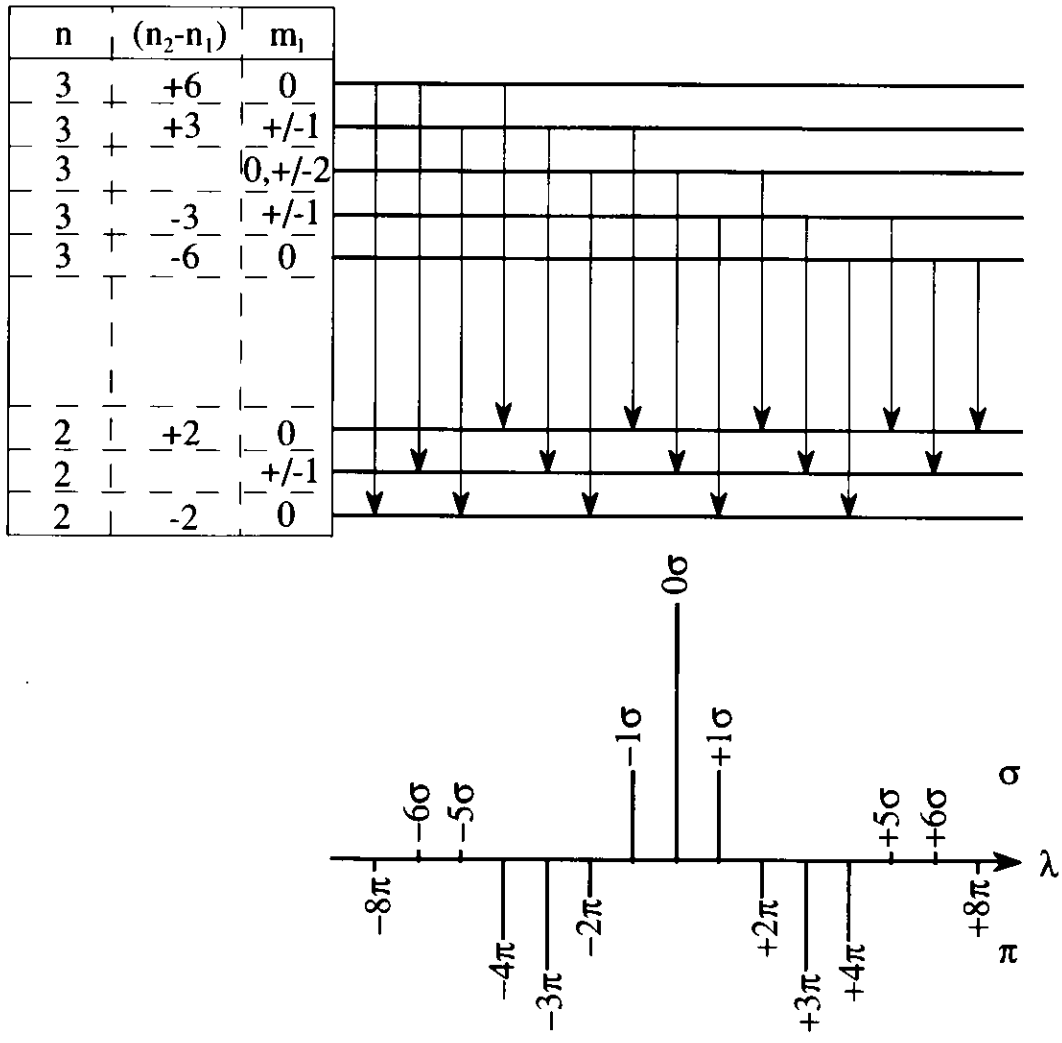

Fig. 1.2.1. Diagram of energy levels and dominant transition processes relevant to the Stark effect of H_α emission on the relative level populations. The n is the principal quantum number. The $n_{1,2}$ and m_1 is also quantum number, which satisfy the relation of $n = m_1 + n_1 + n_2 + 1$.

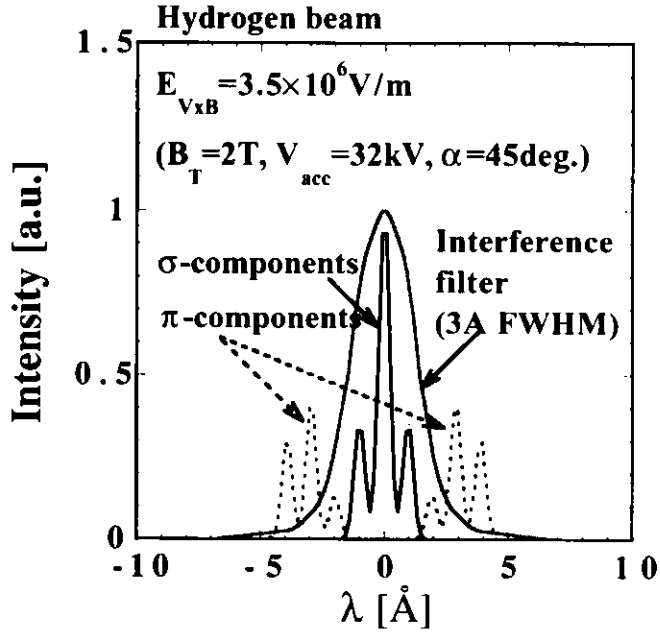

Fig. 1.2.2. Simulation of full energy Stark spectrum for a 32 keV hydrogen beam. Magnetic field 2 T, beam velocity component perpendicular to the magnetic field 2.5x 10^6 m/s (electric field 3.5x10^6 V/m). Observation direction along the magnetic field. Each component of the line was artificially broadened (A linewidth of 0.5 Å is assumed). The filter profile with an 3 Å FWHM is also shown.

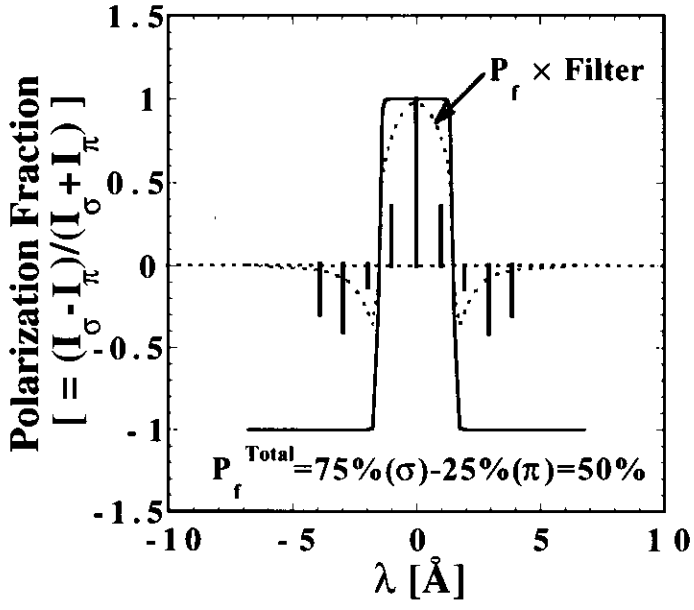

Fig. 1.2.3. Stark effect pattern of the Balmer-alpha (H_α) transition is shown with the vertical bars. The solid curve is the numerically computed polarization fractional profile. The dashed curve is also numerically computed polarization fractional profile based on the convolution of the Stark effect pattern and the filter profile, which shows that total polarization fraction of ~ 50 % will be measured with an 3 Å FWHM filter in this condition.

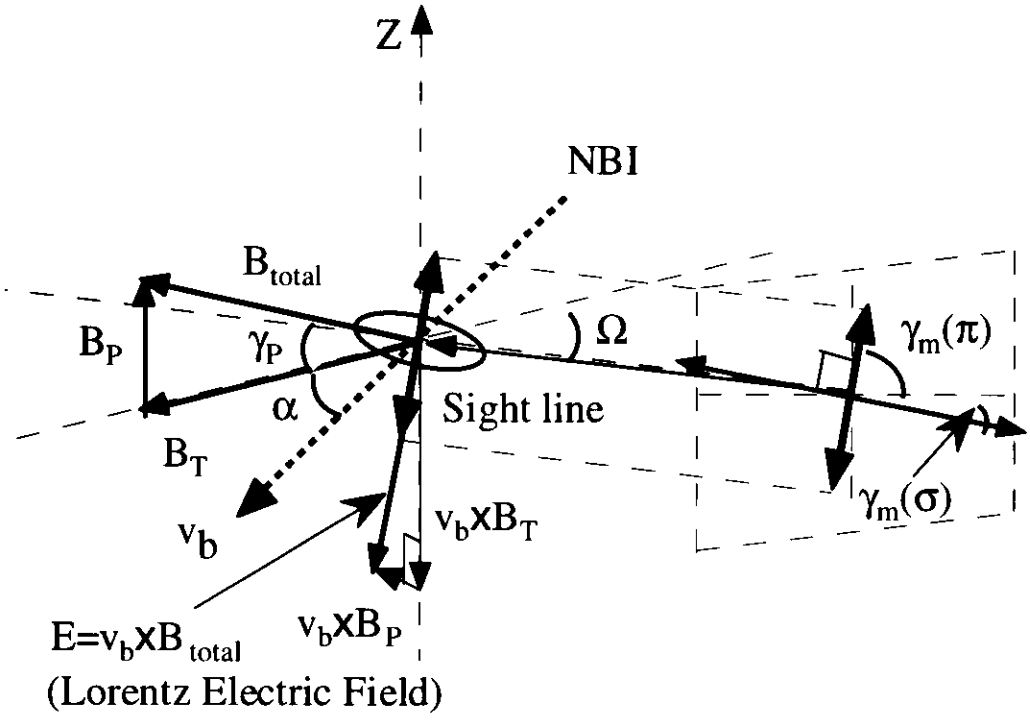

Fig. 1.2.4. MSE viewing geometry, including both the $\mathbf{v_b x B_T}$ and the $\mathbf{v_b x B_p}$ component of Lorentz electric field ($\mathbf{v_b x B_{total}}$). The viewing sightline and neutral beam line (NBI) are in near midplane of the device. The γ_p is the magnetic field pitch angle. The $\gamma_m(\sigma)$ and the $\gamma_m(\pi)$ are σ and π components of measured polarization angle, respectively.

1.3 Modulation technique

The direction of the local magnetic field in a tokamak is deduced from a measurement of the direction of polarization of Stark σ components. In general, the plasma radiation at the Doppler-shifted wavelength of the σ manifold also contains contributions from linearly polarized π components (with polarization direction orthogonal to the σ radiation) and from the unpolarized background. In order to determine the magnetic field pitch angle, only the direction of the σ (or π) components must be measured.

The measurement technique is based on high-frequency modulation of the direction of polarization, conversion of polarization modulation to intensity modulation, and phase-sensitive detection of the modulation amplitude [10, 13]. A schematic of the polarimetry system is shown in Fig. 1.3.1. Two photoelastic modulators (PEMs) are the main component of the polarization analyzer and consist of a birefringent material, such as fused silica, driven at its resonant frequency ($\leq$ 50 kHz) by a piezoelectric transducer. Due to birefringence effects the two transverse refractive indices n_x and n_y, and the difference $n_x - n_y$, vary in time. This result in a time-varying phase shift, $\Delta\Phi$, between the transmitted wave components, $\mathbf{E}_x$ and $\mathbf{E}_y$, of the electromagnetic wave. The phase shift is related to the indices of refraction by

$$\Delta\Phi(t) = (2\pi d/\lambda) / (n_x - n_y) , \qquad (1\text{-}3\text{-}1)$$

where d is the device thickness and λ is the wavelength. The modulation of the phase shift from the PEM is sinusoidal and can be written as

$$\Delta\Phi(t) = \Phi_0 \cos(\omega t) , \qquad (1\text{-}3\text{-}2)$$

where ω is the PEM resonant frequency and Φ_0 is the retardation amplitude determined

by the driven voltage on the transducer coupled to the PEM. The change of phase shift modifies the polarization of the incident light. The PEMs are followed by a linear polarizer that transforms the polarization direction modulation into intensity modulation.

The expected modulation intensity can be calculated using a Stokes vector description of the Stark emission, and Jones (or Muller) matrices for the optical components. Consider light that is linearly polarized at an angle γ with respect to the horizontal axis (X-axis). As shown in Fig. 1.3.1, two photoelastic modulators (PEMs) are oriented with their axes at 45° and 0° to the horizontal, and followed by a polarizer with its polarization direction at 22.5° to the horizontal. The incident polarized wave vector is given by

$$E_0 = \begin{pmatrix} x_0 e^{-i\omega t} \\ y_0 e^{-i\omega t} \end{pmatrix}, \tag{1-3-3}$$

where both x_0 and y_0 are the complex number, and ω is the angular frequency. Several matrices are defined as follows,

$$T(\theta) = \begin{pmatrix} \cos\theta & \sin\theta \\ -\sin\theta & \cos\theta \end{pmatrix}, \tag{1-3-4}$$

$$A_i = \begin{pmatrix} e^{i\phi_i/2} & 0 \\ 0 & e^{-i\phi_i/2} \end{pmatrix}, \tag{1-3-5}$$

$$B = \begin{pmatrix} 1 & 0 \\ 0 & 0 \end{pmatrix}. \tag{1-3-6}$$

Considering the coordinates and the arrangement of each optical element, the transmitted wave vector is obtained by multiplying together the above matrices

$$E_1 = T\left(\frac{\pi}{8}\right)BT\left(-\frac{\pi}{8}\right)A_2T\left(\frac{\pi}{4}\right)A_1T\left(-\frac{\pi}{4}\right)E_0. \tag{1-3-7}$$

The transmitted light intensity behind the polarizer is given by

$$\begin{aligned} I_1 &\propto E_1E_1^* \\ &= \frac{1}{2\sqrt{2}}\left\{\sqrt{2}I + \left[(\cos\phi_1 + \sin\phi_1\sin\phi_2)Q \right.\right. \\ &\quad \left.\left. -\cos\phi_2 U + (\sin\phi_1 - \cos\phi_1\sin\phi_2)V\right]\right\}, \end{aligned} \tag{1-3-8}$$

where I, Q, U, and V are the element of a Stokes vector as

$$S = \begin{pmatrix} I \\ Q \\ U \\ V \end{pmatrix} = \begin{pmatrix} x_0x_0^* + y_0y_0^* \\ x_0x_0^* - y_0y_0^* \\ x_0y_0^* + x_0^*y_0 \\ (x_0y_0^* - x_0^*y_0)i \end{pmatrix}. \tag{1-3-9}$$

Making use of the expansions by Bessel series of $J_n(z)$ as

$$\begin{aligned} \cos\delta &= \cos[\Phi_0\cos(\omega t)] \\ &\cong J_0(\Phi_0) - 2J_2(\Phi_0)\cos 2\omega t + \cdots, \\ \sin\delta &= \sin[\Phi_0\cos(\omega t)] \\ &\cong 2J_1(\Phi_0)\cos\omega t + \cdots, \end{aligned} \tag{1-3-10}$$

resulting in an intensity modulation at harmonics of the drive frequency as,

$$E_1E_1^* \sim \frac{1}{2}\left\{1+\frac{1}{\sqrt{2}}\left[J_0(\Phi_1)Q-J_0(\Phi_2)U\right]\right\}$$
$$+\frac{1}{\sqrt{2}}\left[J_1(\Phi_1)\cos(\omega_1 t)-J_0(\Phi_2)\cos(\omega_2 t)\right]V$$
$$-\frac{1}{\sqrt{2}}\left[J_2(\Phi_1)\cos(2\omega_1 t)Q-J_2(\Phi_2)\cos(2\omega_2 t)U\right]$$
$$+\cdots \text{higher}-\text{harmonics}. \qquad (1\text{-}3\text{-}11)$$

If the incident light is polarized linearly at an angle of γ as

$$E_0=E_0[\cos(\gamma)x+\sin(\gamma)y]e^{-i\omega t}, \qquad (1\text{-}3\text{-}12)$$

then the element of a Stokes vector as

$$I=E_0^2,\ Q=E_0^2\cos(2\gamma),\ U=E_0^2\sin(2\gamma),\ V=0. \qquad (1\text{-}3\text{-}13)$$

As shown in Eq. 1-3-11, both Q and U are the modulation amplitudes of PEMs at $2\omega_1$ and $2\omega_2$, respectively, and can be determined using a lock-in amplifier referenced to the appropriate frequency. The polarization angle is obtained as

$$\tan 2\gamma = \frac{U}{Q}. \qquad (1\text{-}3\text{-}14)$$

On the other hand, the element of a Stokes vector for the unpolarized light are expressed as

$$I=E_0^2,\ \langle Q\rangle=\langle U\rangle=0,\ V=0, \qquad (1\text{-}3\text{-}15)$$

then the unpolarized light is not contribute to the modulation amplitudes of PEMs at $2\omega_1$ and $2\omega_2$, respectively.

The analysis of the operation of the system is complicated by the presence of a mirror in front of the polarimeter, which introduces a differential attenuation and phase shift to the S and P polarization components (where the S-plane is normal to the incident polarization light and the P-plane contains the incident ray and mirror normal).

The transmitted intensity in this case is

$$I' = P_f\left(r_p^2\cos^2\gamma + r_s^2\sin^2\gamma\right) + \left(1 - P_f\right)\frac{\left(r_p^2 + r_s^2\right)}{2}$$
$$= P_f\frac{r_s^2}{2}\left[\left(1 + r_{ps}^2\right) - \left(1 - r_{ps}^2\right)\cos 2\gamma\right] + \left(1 - P_f\right)\frac{r_s^2\left(1 + r_{ps}^2\right)}{2},$$

(1-3-16)

$$U' = r_p r_s\cos\left(\delta_p - \delta_s\right)\sin 2\gamma$$
$$= r_s^2 r_{ps}\cos\delta\sin\gamma,$$

(1-3-17)

$$Q' = P_f\left(r_p^2\cos^2\gamma - r_s^2\sin^2\gamma\right) + \left(1 - P_f\right)\frac{\left(r_p^2 - r_s^2\right)}{2}$$
$$= P_f\frac{r_s^2}{2}\left[\left(-1 + r_{ps}^2\right) + \left(1 + r_{ps}^2\right)\cos 2\gamma\right] + \left(1 - P_f\right)\frac{r_s^2\left(-1 + r_{ps}^2\right)}{2},$$

(1-3-18)

$$V' = -r_p r_s\sin\left(\delta_p - \delta_s\right)\sin 2\gamma$$
$$= -r_s^2 r_{ps}\sin\delta\sin\gamma,$$

(1-3-19)

where P_f is the polarization fraction, δ_p and δ_s is the phase shift of the S and P polarization respectively, r_p and r_s is the reflectivity of the S and P polarization respectively, δ and r_{ps} is the phase difference and reflectivity ratio between the S and P polarization respectively, and the normalization with respect to I is denoted by '. Finally, the polarization angle is obtained as

$$\tan 2\gamma = \frac{2r_{ps}}{\cos\delta}\frac{U'}{\left\{Q'\left(1 + r_{ps}^2\right) + I'\left(1 - r_{ps}^2\right)\right\}}.$$

(1-3-20)

If the r_{ps} is negligibly small, then the above relation can be approximated as

$$\tan 2\gamma \sim \frac{1}{\cos\delta}\frac{U'}{Q'}. \tag{1-3-21}$$

As shown in Eq. 1-3-11, both Q' and U' are also the modulation amplitudes of PEMs at $2\omega_1$ and $2\omega_2$, respectively, and can be determined using a lock-in amplifier referenced to the appropriate frequency. Although the difference in P to S reflectivity can be reduced to a level of less than 1 % over the entire range of angles during manufacturing, the phase shift must be calibrated for incident angles to the mirror.

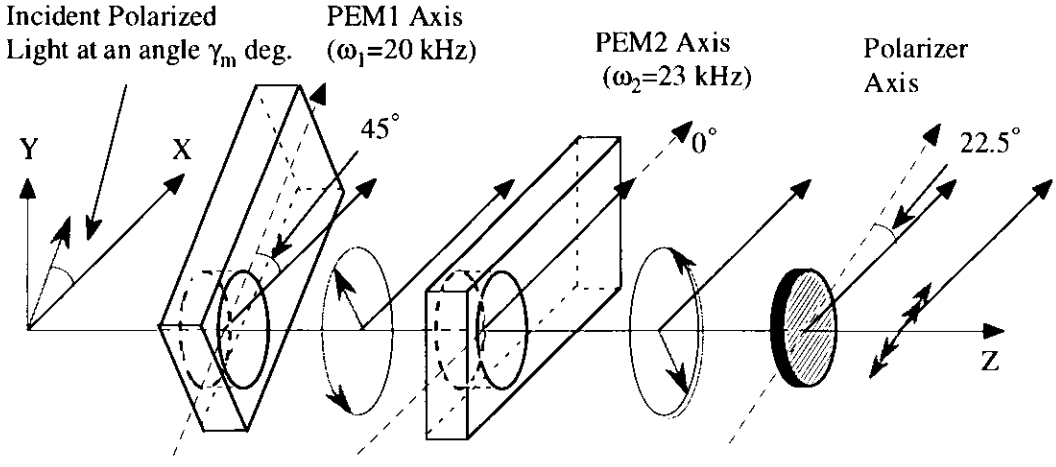

Fig. 1.3.1. Schematic of modulated polarization analyzer. Two photoelastic modulators (PEMs) are oriented with their axes at 45° and 0° to the horizontal. These are followed by a polarizer with its polarization direction at 22.5° to the horizontal. Incident polarized light at an angle γ is also shown.

1.4 Effect of radial electric field on MSE measurements

In the standard analysis, effect of the radial electric field (E_r) on the measured polarization angle was ignored as $E_r << E_L$. However, in a recent experiments with high powered neutral beam injection, a large toroidal rotation and pressure gradient are excited in the plasma (especially, in improved confinement mode such as H-mode), and a large E_r which can be up to a few tens % of the $\mathbf{v_b x B_Z}$ term in Eq. 1-2-1 is formed through the radial force balance as

$$E_r = (Z_i e n_i)^{-1} + \nabla p_i - v_{\theta i} B_T + v_{\phi i} B_P \,, \qquad (1\text{-}4\text{-}1)$$

where Z_i is the charge of ion, p_i is the ion pressure, n_i is the ion density, e is the electronic charge, $v_{\theta i}$ and $v_{\phi i}$ are the ion poloidal and toroidal rotation velocities, respectively [14, 15]. In this case, it is necessary to include the additional term of E_r in Eq. 1-2-1, and which is modified as

$$\tan(\gamma_m) = \{ v_b B_z \cos(\alpha+\Omega) + E_r \cos(\Omega) \} / v_b B_T \sin(\alpha) \,. \qquad (1\text{-}4\text{-}2)$$

Eq. 1-4-2 shows the need for precise pitch angle measurement to correct the effect of E_r measured by other diagnostic tool such as charge-exchange recombination spectroscopy (CXRS) or heavy ion beam probe (HIBP). But the sensitivity to E_r by the Stark effect provides the direct technique of E_r measurement using MSE if additional MSE system is available simultaneously, which has different viewing geometry and/or views different beam energy. Measurement of E_r is also important understanding the physics of high performance plasma confinement such as H-mode through the turbulence suppression by $\mathbf{E_r x B}$ shear flow [16].

Simultaneous measurements of γ_p and E_r are recently demonstrated on DIII-D and TFTR tokamaks by using different methods each other [17, 18]. In the DIII-D MSE

system, it uses the method viewing one neutral beam line from different viewing angle, one is at $\Omega \sim 0°$ (in this geometry, the effect of E_r is maximum as shown in Eq. 3) and the other is $\Omega \sim 90°$ (in this geometry, the effect of E_r is negligibly small) . In the TFTR MSE system, it uses the method viewing different beam energy of one neutral beam line from same viewing angle, one is the full-energy and the other is the half-energy. The DIII-D method has good sensitivity in E_r, but poor spatial resolution. The TFTR method has the advantage of using same sight line and collection optics keeping a good spatial resolution, but uncertainty in E_r is large due to the increased beam attenuation of half-energy component. In the JFT-2M tokamak having two neutral beam lines (one is co-parallel to the plasma current and the other is counter-parallel) , the third approach, which has the best sensitivity in E_r and good spatial resolution, is possible by viewing the two beam lines from only one spectroscopic instrument.

The geometry of a typical viewing chord in the JFT-2M system is shown in Fig. 1.4.1. Both $\mathbf{v_b x B_T}$ motional electric fields viewing co and ctr-NBI, especially, are parallel to Z-axis and take the same direction as shown in Fig. 1.4.2 (a) and (b). On the other hand, both $\mathbf{v_b x B_P}$ motional electric fields viewing co and ctr-NBI, especially, are perpendicular to Z-axis and take the opposite direction due to the difference of the direction of the beam velocity vector, which is coupled with the poloidal magnetic field. Therefore the polarization angle viewing co and ctr-NBI, especially, which is approximately proportional to the ratio of the motional electric fields, $v_b B_P$ / $v_b B_T$, show the opposite direction each other. Considering the effect of E_r on MSE polarization angle, $\mathbf{v_b x B_P}$ motional electric field viewing co-NBI is weakened (or strengthened) by the positive (or negative) E_r, while $\mathbf{v_b x B_P}$ motional electric field viewing ctr-NBI is strengthened (or weakened) by the positive (or negative) E_r. Thus, through the change in

the polarization angle to the opposite direction each other, a maximum separation of the magnetic field pitch angle and E_r can be obtained using both co and ctr-NB lines.

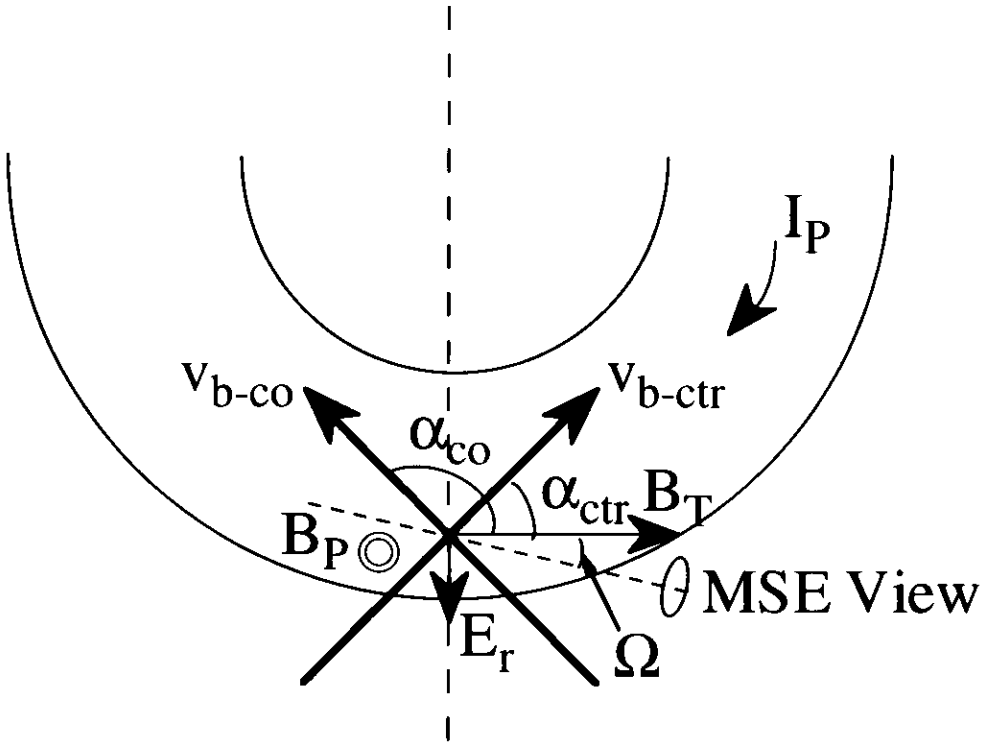

Fig. 1.4.1. MSE viewing geometry on JFT-2M, indicating the radial electric field, E_r.

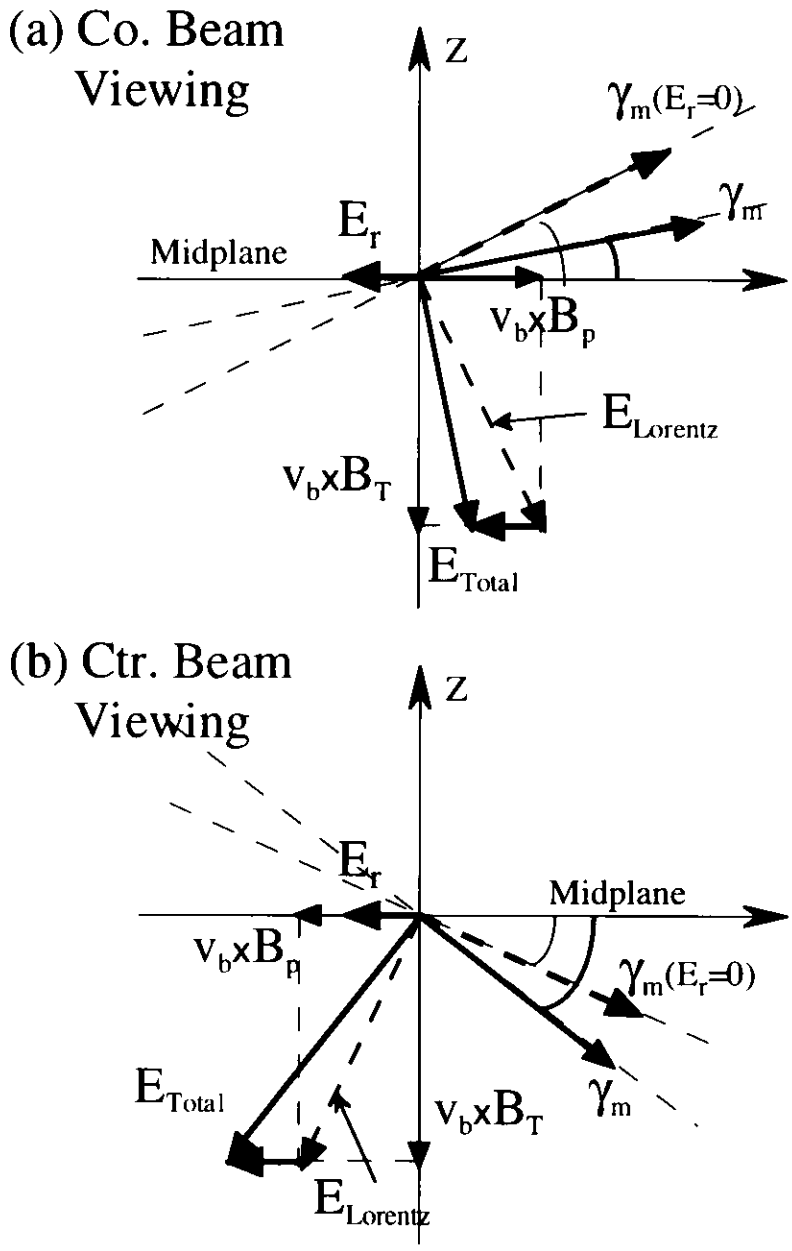

Fig. 1.4.2. Schematic views of MSE geometry viewing (a) co-NBI and (b) ctr-NBI along the line of sight in the case of counter clockwise (CCW) direction of the toroidal magnetic field and clockwise (CW) direction of the plasma current as shown in Fig. 1.4.1.

1.5 JFT-2M tokamak

JFT-2M is a medium size tokamak with a D-shaped vacuum vessel of a major radius R = 1.31 m and a minor radius a ≤ 0.35 m as shown in Fig. 1.5.1. As given in Table 1, the maximum toroidal field at R =1.31 m (B_T) and elongation (κ) are 2.2 T and 1.7, especially. The poloidal coil system on JFT-2M makes it possible to create various plasma shapes including limiter, upper and lower divertor configurations. Additional heating experiments are performed with two hydrogen neutral beam injection (NBI) systems (as given in Table 2) and electron cyclotron resonance frequency heating (ECRH) system set at a frequencies of 60 GHz. A fast wave system is also installed for non-inductive current drive (FWCD) and plasma start-up with low loop voltage. Advanced Material Tokamak EXperiment (AMTEX) is being performed, where compatibility of ferritic steel with plasma is tested [19].

Major diagnostics that are used in this work are as follows (toroidal arrangements of diagnostics and heating systems are indicated in Fig. 1.5.2). The line averaged electron density is measured by 2mm μ wave interferometer from the chord passing through nearly magnetic axis. The electron temperature is measured by electron cyclotron emission (ECE) diagnostic. The profile of the toroidal rotation velocity is measured with charge-exchange recombination spectroscopy (CXRS) using CVI charge-exchange line emission. The profile of the soft X-ray emission is measured by an array of 24 PIN photodiodes as shown in Fig. 1.5.3.

The paper is organized as follows. In chapter 2, the detailed design of the MSE system installed on JFT-2M and calibration of instruments are explained. In chapter 3, equilibrium reconstruction method using CUPID code is discussed. In chapter 4, experimental results of measurements of profiles of the current density and the safety factor in plasma with current ramp and sawtooth activity are described. Preliminary data of E_r measurement in L-mode plasma is also presented. In chapter 5, these results are discussed and this work is summarized.

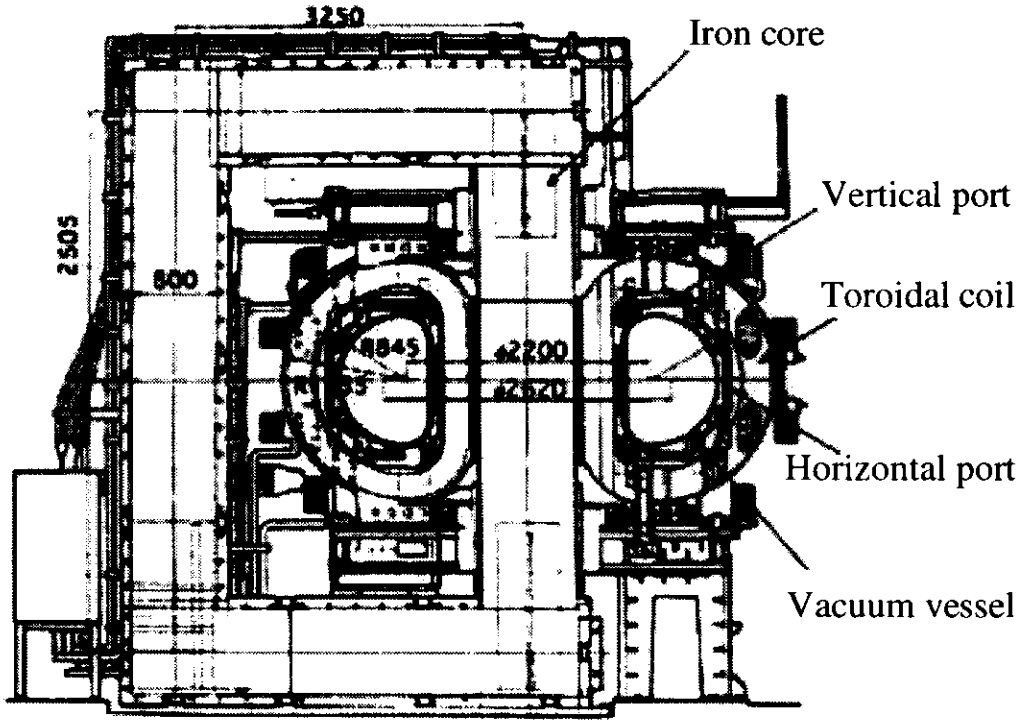

Fig. 1.5.1. Cross-section of JFT-2M tokamak

Table 1. Device parameters of JFT-2M tokamak

Parameter	Value
Major radius, R	1.31 m
Minor radius, a	≤ 0.35 m
Plasma current, I_P	≤ 0.5 MA
Toroidal magnetic field, B_T	≤ 2.2 T
Elongation, κ	≤ 1.7

Table 2. Parameters of Heating NBI system

Parameter	Value
Acceleration voltage, V_{acc}	≤ 40 kV
Beam current, I_{acc}	≤ 65 A
Beam species	Hydrogen
Pulse width	≤ 0.3 sec
Injection angle	Near horizontal and near tangential
Beam cross section	30 cm (vertical) x 12 cm (horizontal)

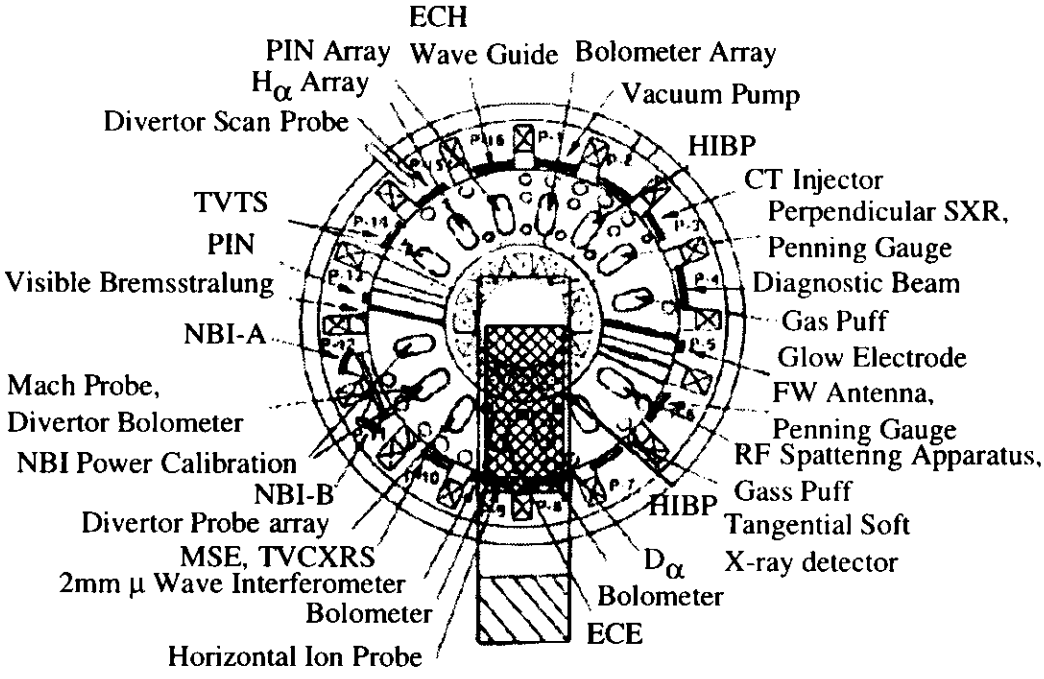

Fig. 1.5.2. Diagnostics on JFT-2M

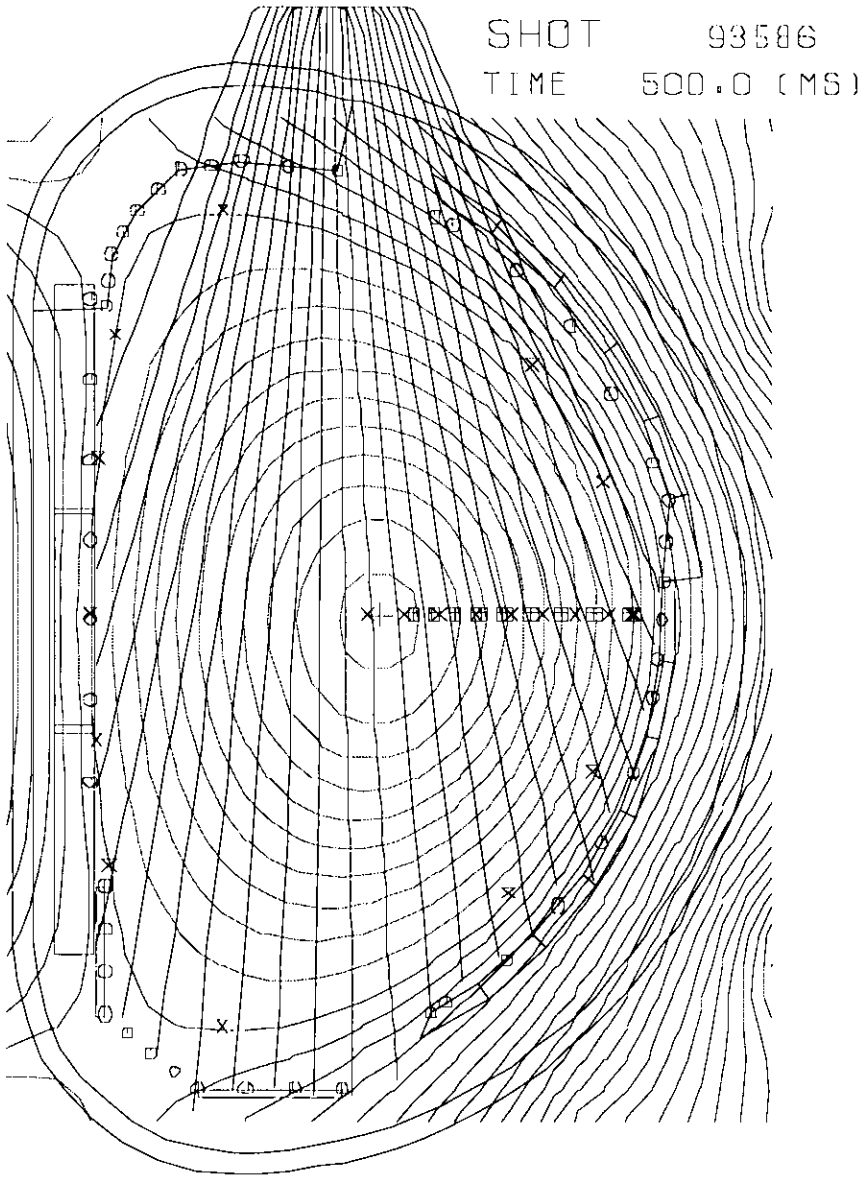

Fig. 1.5.3. Viewing chords of PIN photodiode array. The location of MSE measurements viewing NBI-A and B are also denoted by box-plus symbols and (x), respectively. The magnetic surfaces are reconstructed by EQFIT-code.

Chapter 2

Experimental apparatus

2.1 Motional Stark effect diagnostic system

The instrument consists of the collection optics with a multi-layer dielectric coated mirror, polarimeter (two photo elastic modulators, PEMs, and polarizer), fiber optic link, wavelength filter and photomultiplier detector. Fig. 2.1.1 shows the diagnostic location, neutral beam lines (NBI-B is co-parallel to the plasma current and NBI-A is counter-parallel), and sightlines. The diagnostic can measure the polarization angle at 18 radial location (9 channels per each NBI lines), which cover a region between just inside from the magnetic axis and the outboard edge of the plasma. Viewing both beam lines simultaneously and near tangential to the toroidal magnetic field provide it good spatial resolution and the best sensitivity in E_r measurements. Referring to the geometry shown in Fig. 2.1.2, the radial resolution is given by

$$\delta R = (d \sin \alpha + W \sin \Omega) / \sin(\alpha+\Omega) , \qquad (2\text{-}1\text{-}1)$$

where d is the optical spot size (1 cm) and W is the full width of half maximum (FWHM) of the beam (12 cm). This function is plotted in Fig. 2.1.3 for both NBI-A (solid line) and NBI-B (dashed line). These have a good radial resolution of about a/10 (a is the minor radius), except for the central channel of NBI-A's system. As shown in Fig. 2.1.4, the collection optics with 7 lenses consisting of a zero Verdet constant [20] glass and a multi-layer dielectric coated mirror, polarimeter (two photo elastic modulators, PEMs, and polarizer) and fiber optic array are installed on the front of the

viewing port (these are located just outside of the vacuum vessel). The size of the clear aperture on PEMs is 10 cm, with resonant frequencies of 20 and 23 kHz. In this work, two photoelastic modulators are oriented with their axes at 22.5° and –22.5° to the horizontal, and followed by a polarizer with its polarization direction at 0° to the horizontal as shown in Fig. 2.1.5. Referring Eq. 1-3-14 described in section 1-3, the polarization angle is evaluated by the normalized difference, ND (the difference of $2\omega_1$ = 2 × 20 kHz and $2\omega_2$ = 2 × 23 kHz lock-in amplifier outputs normalized by sum of them), of the intensity modulation amplitudes at $2\omega_1$ and $2\omega_2$ from lock-in amplifires as

$$\frac{S_2(2\omega_2)}{S_1(2\omega_1)} = \tan 2(\gamma - \frac{\pi}{8}) = \frac{\tan 2\gamma - 1}{1 + \tan 2\gamma}$$
$$\Rightarrow \tan 2\gamma = \frac{S_1(2\omega_1) - S_2(2\omega_2)}{S_1(2\omega_1) + S_2(2\omega_2)}. \qquad (2\text{-}1\text{-}2)$$

The fibers are 0.4 mm core diameter and 0.5 mm cladding diameter and each channel contains 24 fibers arranged with 12 vertical by 2 horizontal (as shown in Fig. 2.1.6). The observed wavelength is far from back ground H_α / D_α line (6563 Å) by more than 30 Å due to Doppler shift and its directions are opposite each other (NBI-A : towards the red, NBI-B : towards the blue). Therefore, the line emission from opposite beam line and back ground light is collimated through a 3 Å FWHM interference filter before being focused onto the photocathod of a photomultiplier (PMT) detector. The filters are individually set for each channel corresponding to its Doppler shifted wavelength and need to be tunable. Also the measured polarized fraction is very sensitive to wavelength (especially, in the case of low B_T discharge) and needs to be set to the central σ components. The filter is tuned by heating it between 25 to 60 °C with filter oven, which shifts the passband of the filter. The shift is about 0.17 Å/°C. This allows a

change of about 6 Å which can cover a hydrogen beam energy of 30 to 36 keV (generally data has been taken at 32 keV). The detectors are Hamamatsu R943-02 with GaAs photocathodes. As shown in Fig. 2.1.7, the detected signals are split into two phased lock-in amplifiers with the reference signals from PEMs. The lock-in amplifier outputs which is approximately proportional to the sine and cosine of the polarization angle are digitized with transient recorder and data acquisition is done by a stand-alone computer.

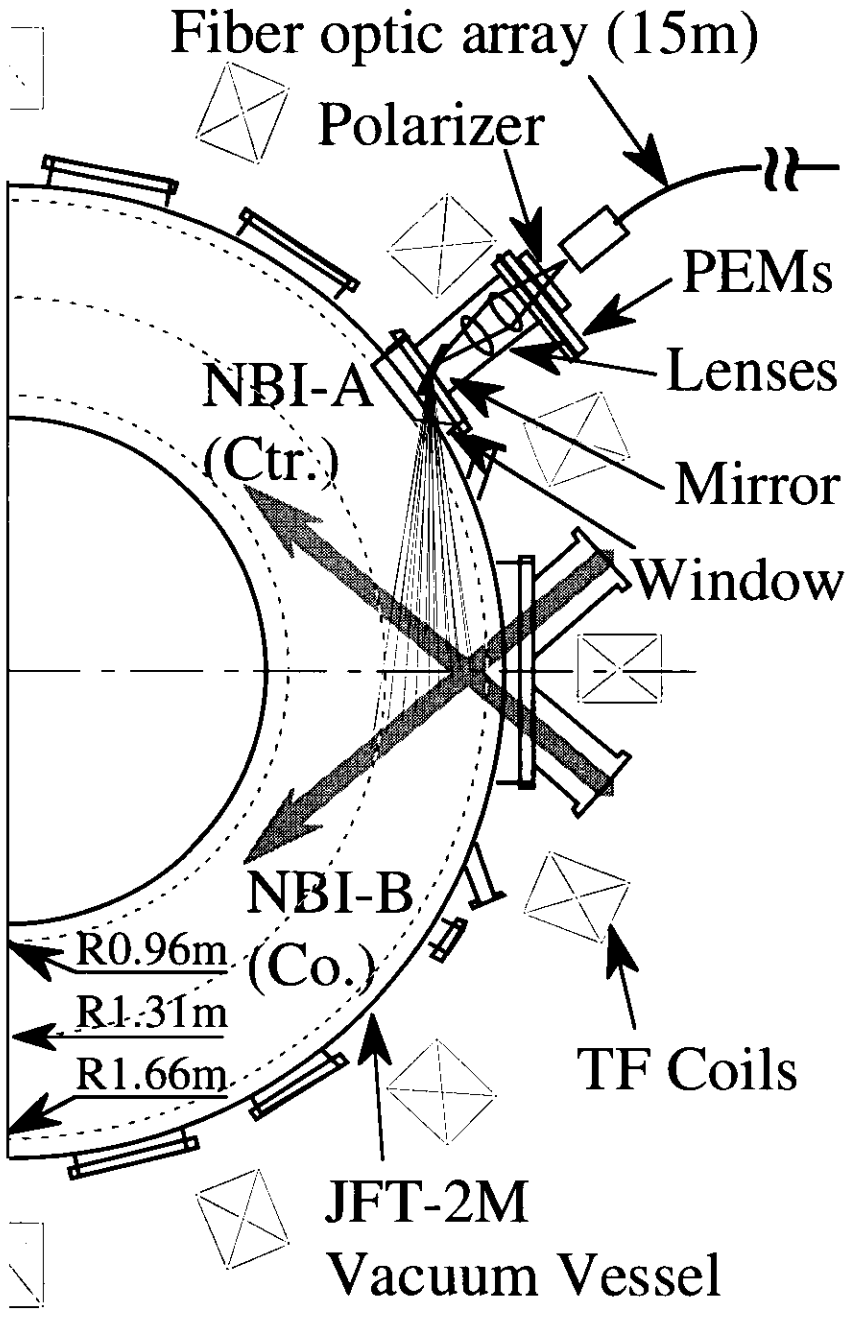

Fig. 2.1.1. Plan view of the JFT-2M tokamak and viewing geometry of the 18 channel MSE system.

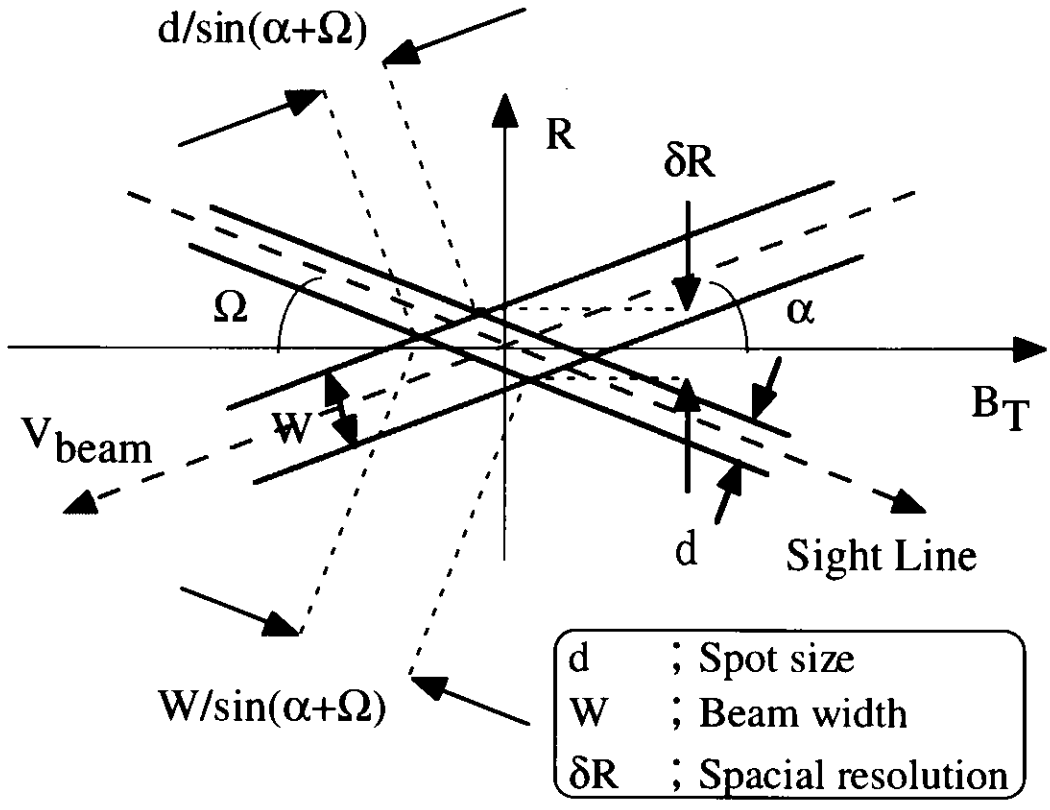

Fig. 2.1.3. Overview of the MSE viewing geometry. B_T is toroidal magnetic field, α is the angle between the viewing sight line and neutral beam line, Ω is the angle between the viewing sight line and the toroidal magnetic field line.

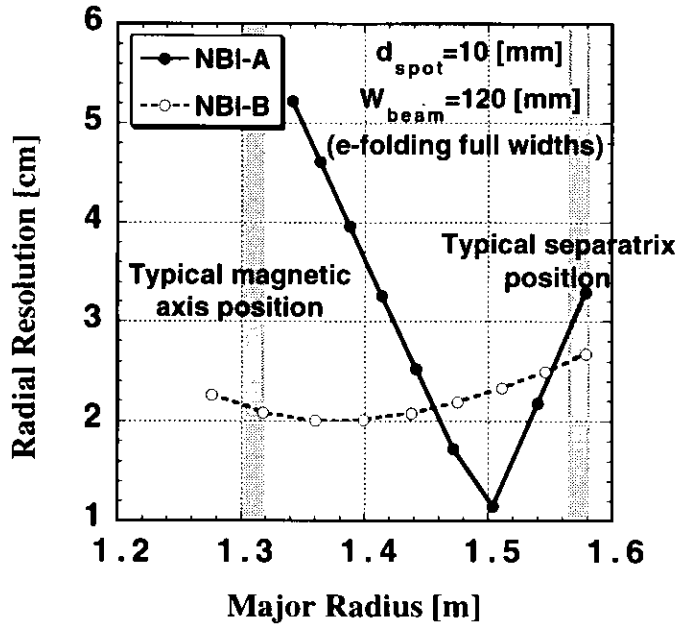

Fig. 2.1.3. Radial resolution vs. radial position for the NBI-A (solid) and NBI-B (dashed) MSE viewing geometry.

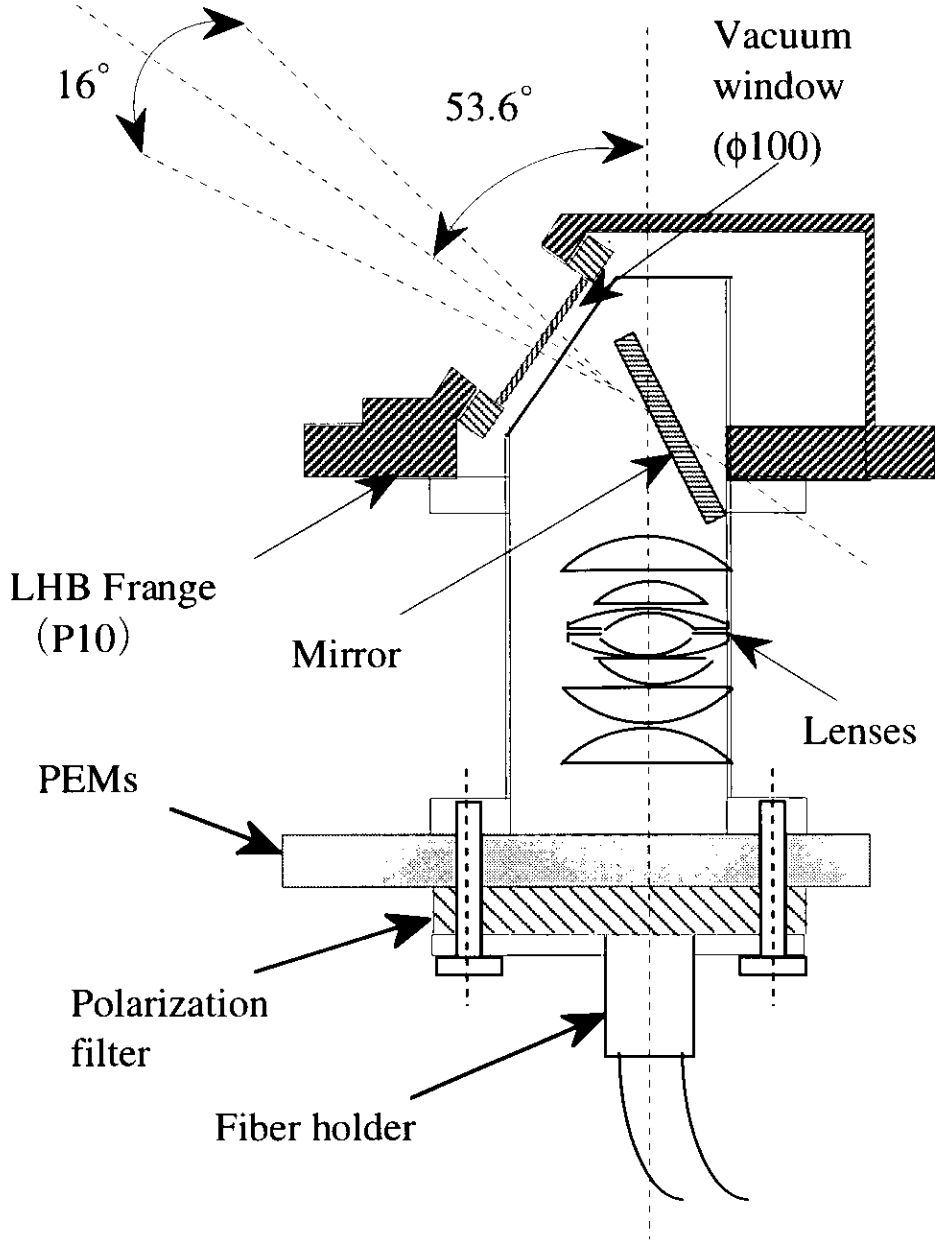

Fig. 2.1.4. Overview of MSE collection optics and polarimeter. A part of port structure with window is also shown.

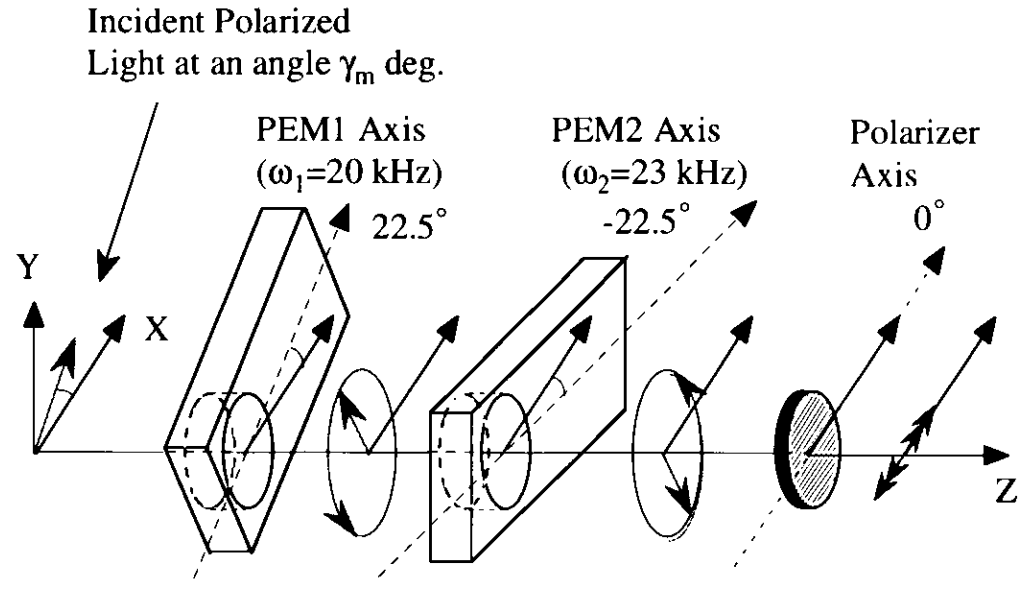

Fig. 2.1.5. Schematic of modulated polarization analyzer. Two photoelastic modulators (PEMs) are oriented with their axes at 22.5° and -22.5° to the horizontal. These are followed by a polarizer with its polarization direction at 0° to the horizontal. Incident polarized light at an angle γ is also shown.

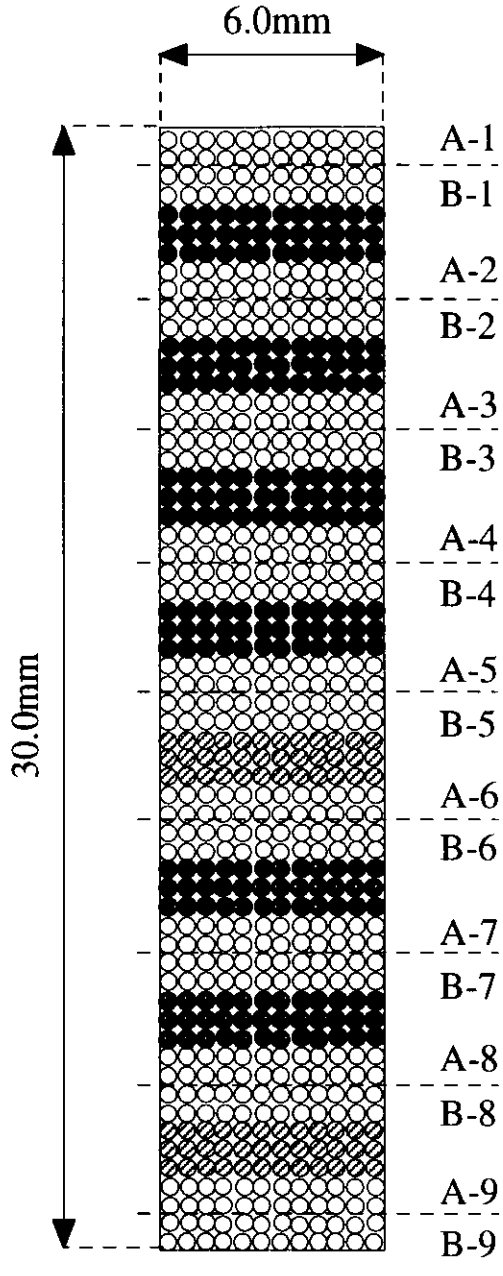

Fig. 2.1.6. Layout of the detection surface of the fiber optics. The fibers are 0.4mm core diameter and 0.5mm cladding diameter. Each channel consists of 24 fibers, arranged with 12 vertical by 2 horizontal fibers, except for reserved channels that are shown by dashed lines. The dummy fibers are denoted by (●).

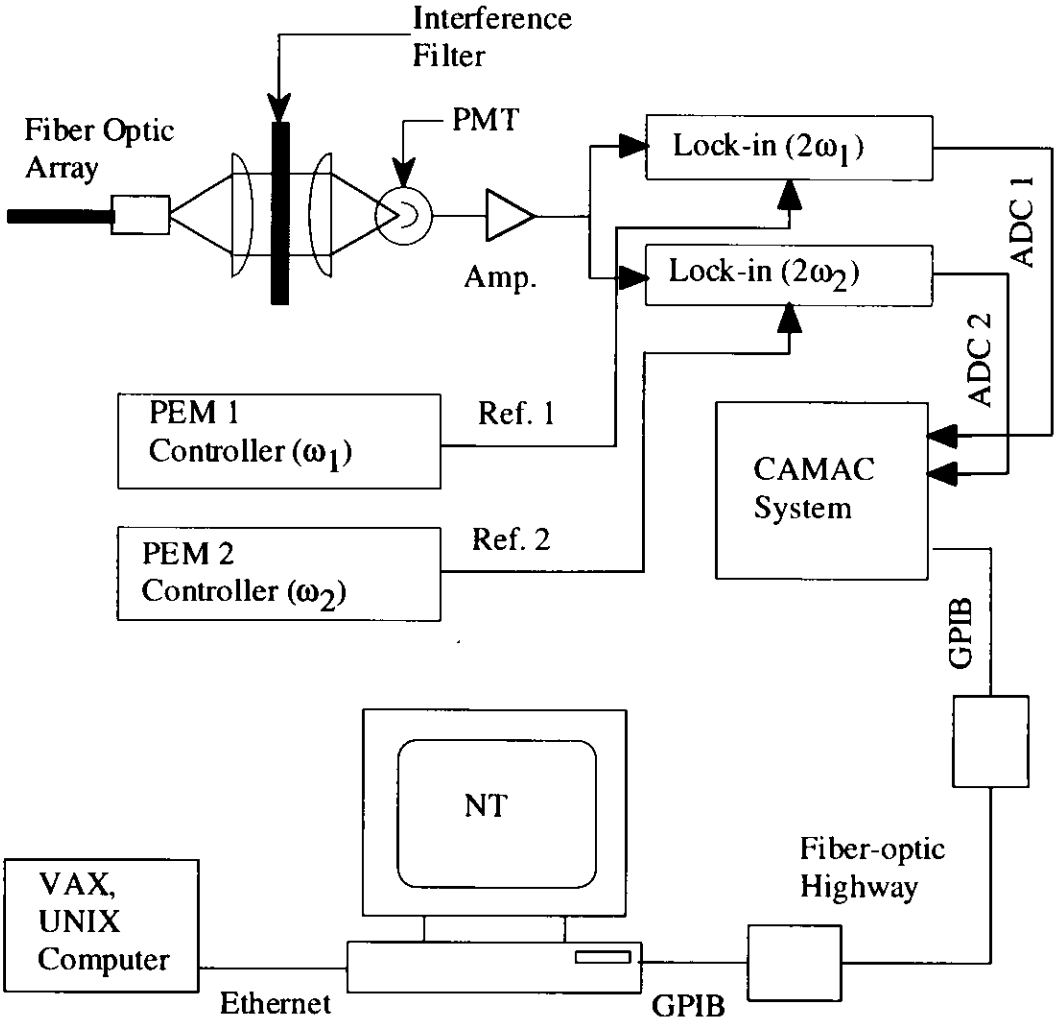

Fig. 2.1.7. Electronics and detector setup (1 of 18 channels). A reference waveform from PEMs is used for the lock-in amplifiers to demodulate the detector signal.

2.2 Calibration of instruments

In the MSE diagnostic, it is required careful calibration for reliable measurement. In the first place, the position of intersections of the sight lines and NBI line must be calibrated. These are inferred from measurements made inside vacuum vessel. In this procedure, the optics is backlighted from the end of the fiber bundle and the positions of sightlines are measured with respect to the focus points in the tokamak.

As shown in Fig. 2.1.4, the design is complicated by the need of reflector to extend the viewing angles. Note its location just outside of the vacuum vessel. A property of all metal reflectors is that the S and P polarization reflect with different amplitude and phase depending on the angle of incidence (where the S-plane is normal to the incident polarization light and the P-plane contains the incident ray and mirror normal). This effect is a serious problem because it can lead to a rotation of the incoming polarization and also polarizes the background plasma light. Calibration of polarimeter is thus very important in the case of collection optics to have the mirror. Although the difference in P to S reflectivity is minimized less than 1 % over the entire range of incidence angles with a multilayer dielectric coating of mirror, the phase shift emerges as the incidence angle is separated from design value. Calibration of polarimeter is performed using an integrating sphere light source with a rotatable polarizer mounted on the aperture, which is placed inside the JFT-2M vacuum vessel. To determine the calibration curve as a function of the input linear polarization angle, the normalized difference, ND (the difference of $2\omega_1 = 2 \times 20$ kHz and $2\omega_2 = 2 \times 23$ kHz lock-in amplifier outputs normalized by sum of them), is plotted as shown in Fig. 2.2.1 (one of 18 channels). These data are fitted with the two-parameter function as

$$ND = m_1 \tan(2m_2\gamma), \qquad (2\text{-}2\text{-}1)$$

where γ is the polarization angle, and m_1 and m_2 are free parameters. Dependence of m_1 and m_2 on the incidence angle are shown in Fig. 2.2.2. It is found that these are inconsistent to the ideal value only 10 % as expected. These calibration values of m_1 and m_2 may offer a good stability and reliability, since it is obtained in near same condition compared with tokamak experiments such as temperature of environment.

Calibration of offset angle is a very important element to the successful implementation of this technique. A nonzero offset angle is due to the magnetic field of the tokamak, which produces rotation of the polarization direction in the optics and vacuum window as described by the Faraday rotation effect. Mechanical misalignment of the instrument with respect to the tokamak can also lead to an observation of a nonzero offset angle. The measurement of the offset angle is performed by injecting the NB pulses of 40 ms into the tokamak with only the toroidal field coils activated, puffing H_e gas into the torus, and no plasma current. The polarization angle is then measured as a function of the toroidal magnetic field, B_T. As shown in Fig.2.2.3, it is found that the offset angle has a weak dependence on the B_T. This is especially important because Faraday rotation correction for the weaker poloidal field such as the radial magnetic field, B_r (which is about two order of magnitude smaller compared with B_T), can be neglected. It is due to the use of a zero Verdet constant glass in optics, however the effect of the Faraday rotation still exists. For example, it may occur in the vacuum window of the 1 cm thick, which is constructed from fused quartz with nonzero Verdet constant. Although the offset angle is obtained by NB injection into the gas-filled torus, the signal to noise ratio is not very good compared with plasma. To reduce the statistical uncertainty, the method of a rapid radial motion of the plasma (RPM) during neutral

beam injection is useful [21]. Fig. 2.2.4 shows time evolution of pitch angle measured by MSE at R = 1.28 m and at R = 1.32 m and the position of magnetic axis calculated by equilibrium code (EQFIT) which includes external magnetic measurement alone in reconstruction. Calibration are performed under the condition of the I_p of 0.25 MA and B_T of 2.2 T with a limiter configuration. The NBI is balanced with $P_{NBI\text{-}A} = P_{NBI\text{-}B} \sim 0.3$ MW. As shown in Fig. 2.2.4, to cross calibrate MSE sightlines, the magnetic axis is moved about 5 cm from t ~ 600 to ~ 650 ms along the midplane by increasing equilibrium field and it keeps the position of R_{axis} ~ 1.27 m after t ~ 650 ms. The pitch angle at R = 1.32 m, which views near magnetic axis before a plasma radial motion, is increased near linearly as the R_{axis} is moved to the high field side. On the other hand, the pitch angle at R = 1.28 m, which views slightly inside from the magnetic axis before a plasma motion, shows near linearly increase as the pitch angle at R = 1.32 m. It is found that the magnetic axis passes through R = 1.28 m at t ~ 650 ms and then the pitch angle at R = 1.28 m shows nearly zero value. Although an absolute value of offset angle is determined by this method, it is limited only a few channels around the magnetic axis. Its difference of neighboring channels $(\gamma_{i+1}^{offset} - \gamma_i^{offset})$ can be determined by subtracting the difference between the calculated angles $(\gamma_{i+1}^{cal} - \gamma_i^{cal})$ from the difference between the measured angles $(\gamma_{i+1}^{mes} - \gamma_i^{mes})$ when it passes through the same flux surface assuming q-value constant,

$$(\gamma_{i+1}^{offset} - \gamma_i^{offset}) = (\gamma_{i+1}^{mes} - \gamma_i^{mes}) - (\gamma_{i+1}^{cal} - \gamma_i^{cal}) . \qquad (2\text{-}2\text{-}2)$$

The absolute value of offset angle is determined using the channel on the magnetic axis, whose polarization angle does not depend on the q-value. Fig. 2.2.5 shows the pitch angle profile vs. major radius. In this figure, all 18 data are mapped together as if the plasma is fixed and the sightlines are moved. By this procedure, it is found that the

uncertainty in the pitch angle measurement is about ~ 0.1 deg. with a time resolution of 10 ms. .

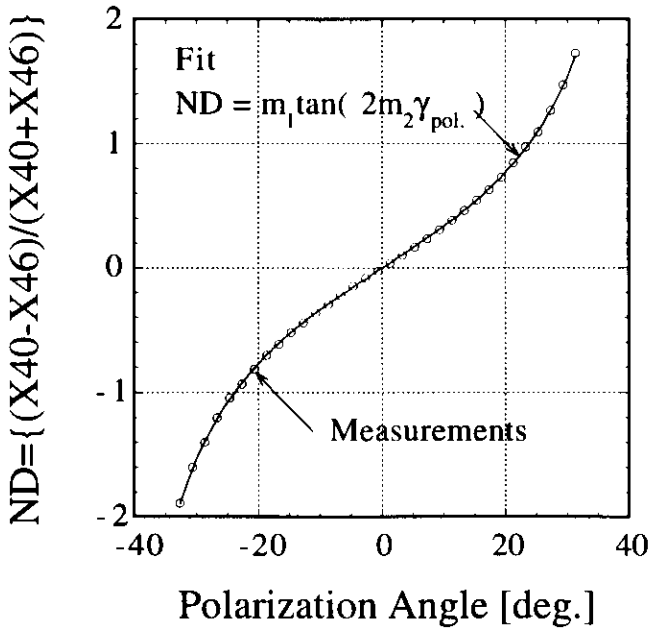

Fig. 2.2.1. Polarimeter calibration curve.

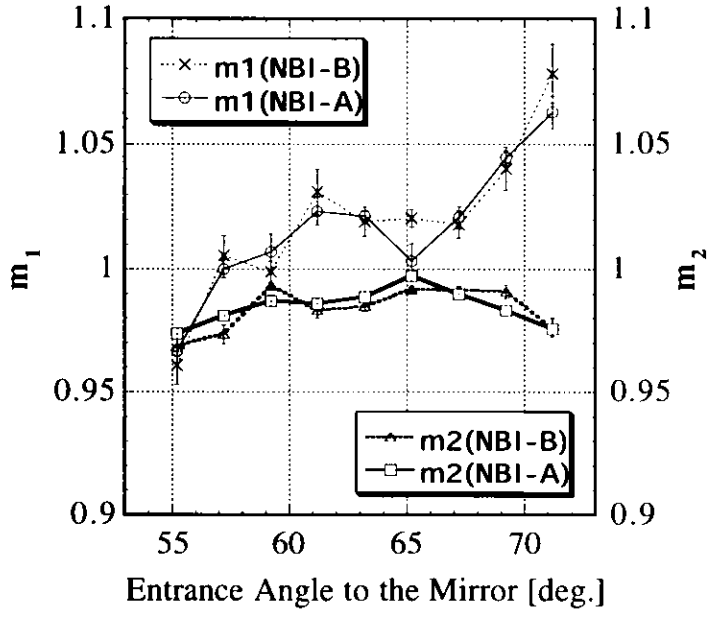

Fig. 2.2.2. Dependence of m_1 and m_2 on the incidence angle.

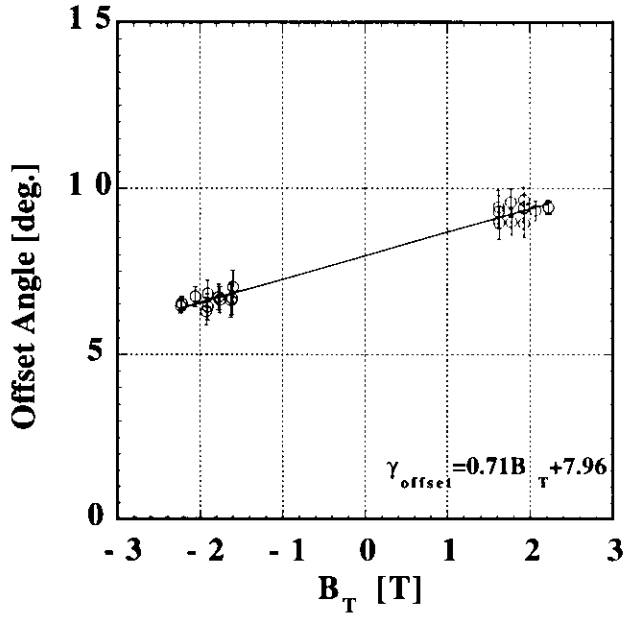

Fig. 2.2.3. An example of the measured dependence of the offset angle on the toroidal magnetic field (B_T). Solid line is the least-squares weighted fit to the experimental points.

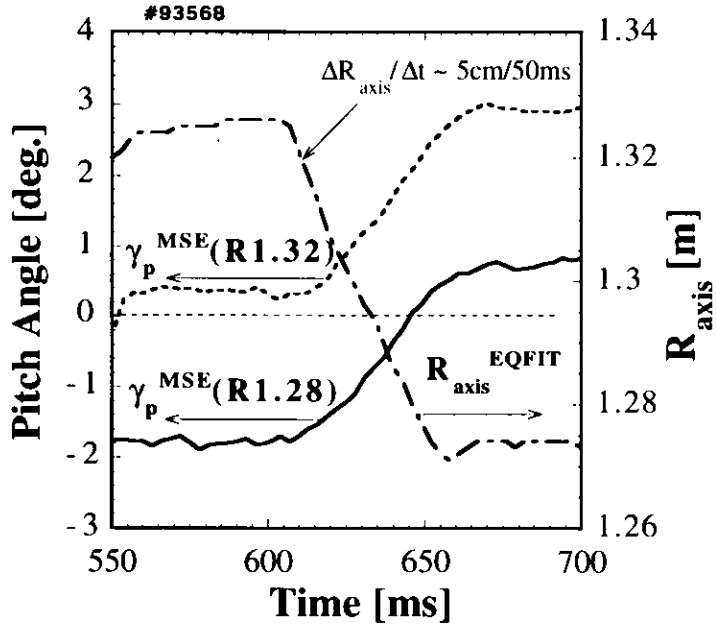

Fig. 2.2.4. Time evolution of pitch angles measured by MSE at R = 1.27 m (solid line) and at R = 1.32 m (dashed line) and the position of magnetic axis (chained line) calculated by equilibrium code (EQFIT) which includes external magnetic measurement alone in reconstruction.

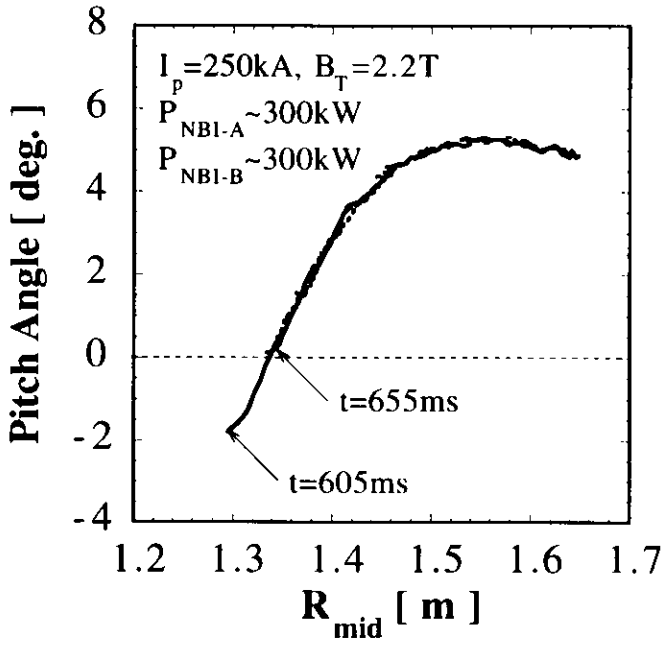

Fig. 2.2.5. The offset calibration by a rapid radial motion of the plasma to cross calibrate sightline. All 18 data are mapped together as if the plasma is fixed and the sightlines are moved. : Solid lines are co-NB-viewing chords and dashed lines are ctr-NB-viewing chords.

Chapter 3

Equilibrium reconstruction

For the tokamak plasma with a circular cross section, the toroidal current density profile j_ϕ may be deduced via Ampere's law from the measured profile of the internal magnetic field pitch angle. The safety factor profile is also evaluate assuming the appropriate function of Shafranov shift of Δ as

$$q(R) = \rho / \{R\tan(\gamma_p)\,[1 + \Delta]\}\,, \qquad (3\text{-}1)$$

where γ_p is the pitch angle and ρ is the radius of the flux surface which is shifted by Δ [21]. For a non-circular plasma shape, the pitch angle profile from MSE measurement is not sufficient to obtain the j and q-profile, because of its dependence on the shape of the flux contours. In order to determine the equilibrium, (i.e. j-profile), and q-profile selfconsistently, the free boundary equilibrium code (CUPID; CUrrent Profile IDentication code) has been introduced on JFT-2M, which solves the Grad-Shafranov equation with the internal magnetic field measured by MSE in conjunction with the information about the shape of the plasma magnetic surfaces. This information is obtained from the magnetic measurements performed just inside the machine vacuum vessel with magnetic probes, flux loops and Rogowski coils (total plasma current and currents in the plasma shaping coils). The Grad-Shafranov equation in a cylindrical coordinate system (R, Z, ϕ)

$$\Delta^* \psi(R, Z) = - \mu_0 R\, j_\phi(R, \psi), \qquad (3\text{-}2)$$

where Δ^* is the operator defined as $R^2 \nabla \cdot (\nabla / R^2)$, $\psi(R, Z)$ is the poloidal flux and j_ϕ is the toroidal current density, is solved by inverting the Δ^* operator, while all the

measured quantities are approximated by minimizing

$$\varepsilon \geq \sum_i w_i \frac{(M_i - C_i)^2}{M_i^2}, \tag{3-3}$$

where C_i and M_i are the computed value, the measured value, and w_i is the weight of the corresponding data. In this work, it takes the ε of ~ 10^{-2} for convergence in Eq. 3-3, and the weights of the MSE, magnetic probe and flux loop data are selected at ~1.0, 1.0 and 130, especially. It means that an iteration process to determine equilibrium is continued till the difference between the computed and measured values at about 10 % for both MSE and magnetic probe data and at 1 % for flux loop.

The j_ϕ is expressed in terms of one dimensional function p' and ff' as

$$j_\phi = Rp'(\psi) + ff'(\psi)/(\mu_0 R), \tag{3-4}$$

where p is the plasma pressure, $f=RB_T$ is the poloidal current enclosed between a flux surface and the magnetic axis, and the differential with respect to ψ is denoted by '. The p' and f functions are specified by the pressure profile and the surface averaged parallel current $\langle j_{//} \rangle$ (= $\langle j_{//} \cdot B \rangle / \langle B \rangle$), respectively. The surface averaged parallel current density and the pressure profile are assumed to have the following functional dependence with the normalized poloidal flux ψ_n :

$$\langle j_{//} \cdot B \rangle = j_0 B_0 [1 + \alpha_1(1 - \psi_n) + \alpha_2(1 - \psi_n)^2 + \alpha_3 \psi_n(1 - \psi_n) + \alpha_4 \psi_n(1 - \psi_n)^2], \tag{3-5}$$

$$p' = p_0'[(1 - \beta_3)(1 - \psi_n^{\beta 1})^{\beta 2} + \beta_3], \tag{3-6}$$

$$\psi_n = (\psi - \psi_{axis}) / (\psi_{surf} - \psi_{axis}), \tag{3-7}$$

where the subscript 0 denotes the value on the magnetic axis and the α and β are linear coefficients that are determined from the measured signals and the imposed constraints (such as total plasma current, I_P). The ψ_{surf} and ψ_{axis} are the poloidal flux at the magnetic

axis and the surface, especially. The edge current density is assumed to be zero since the plasma considered here is L-mode and there is no pedestal structure.

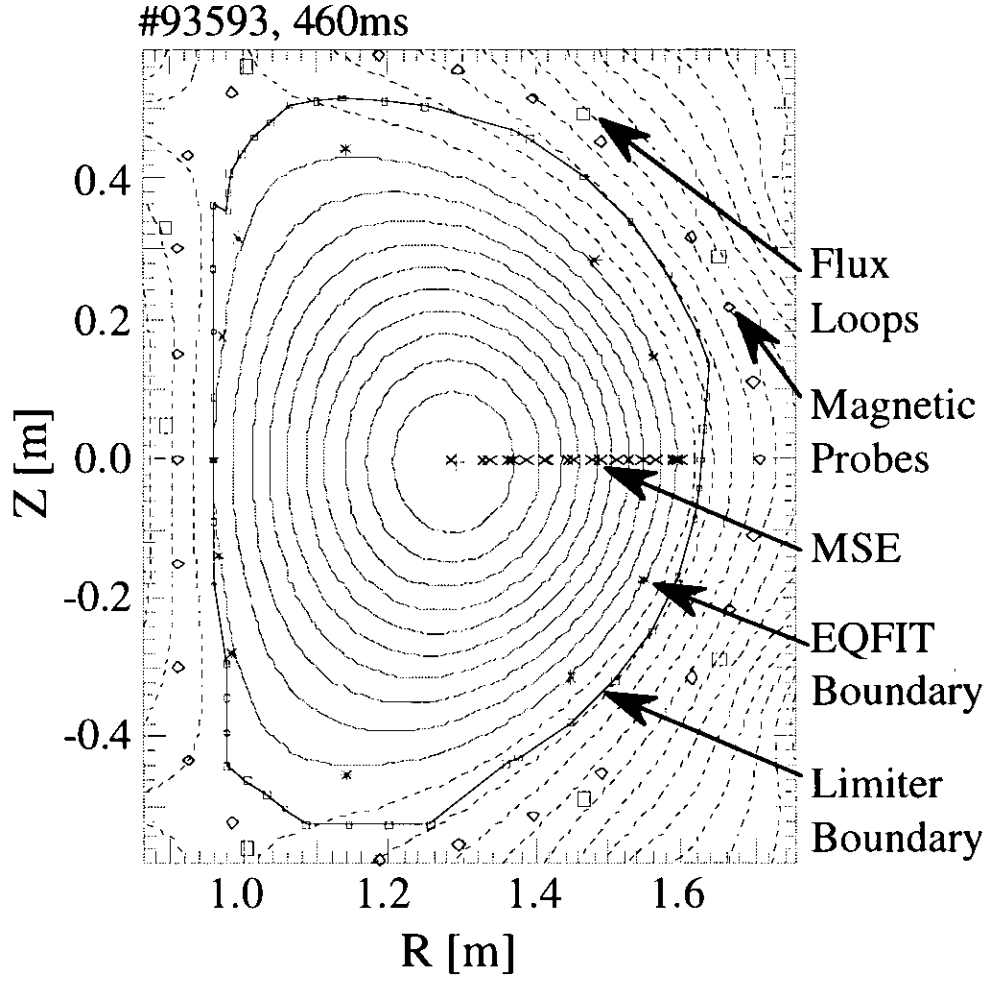

Fig. 3.1. The magnetic surfaces reconstructed by the equilibrium code CUPID with the use of internal MSE measurements. The location of MSE measurements, external magnetic probes and flux loops are denoted by (x), (◇) and (□), especially. The reconstructed plasma boundary points from EQFIT code, which are used for the constraint, are also denoted by (*).

Chapter 4

Experimental results

4.1. Sawteeth

As an example of the performance of the MSE diagnostic, the typical L-mode discharges with sawteeth are shown in Fig. 4.1.1 (a~d). Each discharges have different ramp up rate (dI_P/dt, which are evaluated from 300 to 400 ms) from 1.1 to 1.6 MA/s and the plasma current (I_P) at the flat top (~ 400 ms) are varied from 0.25 to 0.4 MA with fixed B_T of 2.2 T and with a limiter configuration. The balanced NBI with total input power of ~ 0.6 MW is turned on from the ramp up phase of I_P at 300 ms and lasts up to 600 ms. The q(0) values are evaluated by the slope of the pitch angle near the magnetic axis ($s \equiv d\{\tan(\gamma_p)\}/dR$) using the elongation of flux surfaces near the axis (κ_0) and position of the magnetic axis (R_{axis}) from EQFIT as

$$q(0) \approx (\kappa_0/R_{axis})/s \, . \qquad (4\text{-}1\text{-}1)$$

The uncertainty in q(0) is related to the uncertainty in the slope by

$$\delta q(0) \approx (R_0/\kappa_0)\, q(0)^2 \delta s \, . \qquad (4\text{-}1\text{-}2)$$

It clearly shows that the sawtooth crashes emerge reproductively just after the q(0) pass through ~ unity and it remains constant after sawtooth crash as it has reported on many tokamaks [22-25]. Although the dI_P/dt is varied in all discharges, the q(0) takes nearly same value of ~ 2 at the time slices of same I_P of ~ 0.25 MA during ramp up phase. It seems that the plasma currents are ramped up with a monotonic or weak reversed magnetic shear [= 2V/q(dq/dV) where q is the safety factor and V is the flux surface

volume] profile and the q(0) during ramp up phase decrease as surface q values decrease. It is not inconsistent with the result that the sawtooth crashes occur more earlier as the discharges of larger I_P (and smaller surface q values) at the flat top, irrespective of dI_P/dt, however detail profile of safety factor, q(r), must be determined selfconsistently with equilibrium due to its dependence on the shape of the flux contours. The equilibrium calculation including the MSE data is described as follows.

The time evolution of reconstructed j and q-profiles in plasmas shown in Fig. 4.1.1 are indicated in Fig. 4.1.2 ~ Fig. 4.1.4. The first time-slice at 310 ms represents Ohmic and/or initial NB heating phase during the plasma current ramp with different dI_P/dt. It is confirmed that the plasma currents are ramped up with a broad current density profiles. Note the slightly more broad current density profiles as the discharges of smaller I_P (and higher surface q values) at the same time-slice. The next time-slice is 100 ms after the NB turned on, and the plasma currents reach ~ 0.25 (#93589), 0.3 (#93591), 0.35 (#93592) and 0.4 MA (#93593), especially, and show the parabolic current density profiles in all discharges, and the q(0) is seen to decrease as well as the surface q value. In the final time-slice at 510 ms, a significant peaking of current density profiles are found in all discharges, and the q(0) values for discharges of #93592 and #93593 show less than unity. The uncertainty in CUPID reconstructed q(0) is found to be less than ±5 %, which is estimated from random errors of ±0.1° given in central pitch angle data, artificially. There is disagreement [about 30 %, especially for ramp up phase with higher q(0) value] between CUPID reconstructed q(0) and q(0) evaluated by the slope of the central pitch angle using Eq. 4-1-1. Although evaluation of q(0) using Eq. 4-1-1 provides a fast method for obtaining q(0), the uncertainty in q(0) is large at high q(0) in addition to the uncertainty of the flux shape in the core region. It may cause a

quantitative disagreement between reconstructed value. Results of reconstruction are consistent quantitatively with the soft X-ray measurements in term of these discharges having sawtooth activity [the q = 1 radius is about 0.1a (a is minor radius) as well as the inversion radius in the soft X-ray emission]. Also, in discharges of #93589 and #93591 that the sawtooth crash emerges nothing yet at this time-slice, the q(0) values take slightly larger than unity. Although the sawtooth oscillations are not readily visible on the MSE with a fixed time resolution of 10 ms due to the relatively high frequency (100 Hz) and small amplitude of the sawtooth in this examples, it will be improved using more faster time resolution of 1 ms in addition to the application of MSE to the plasma with another MHD activities.

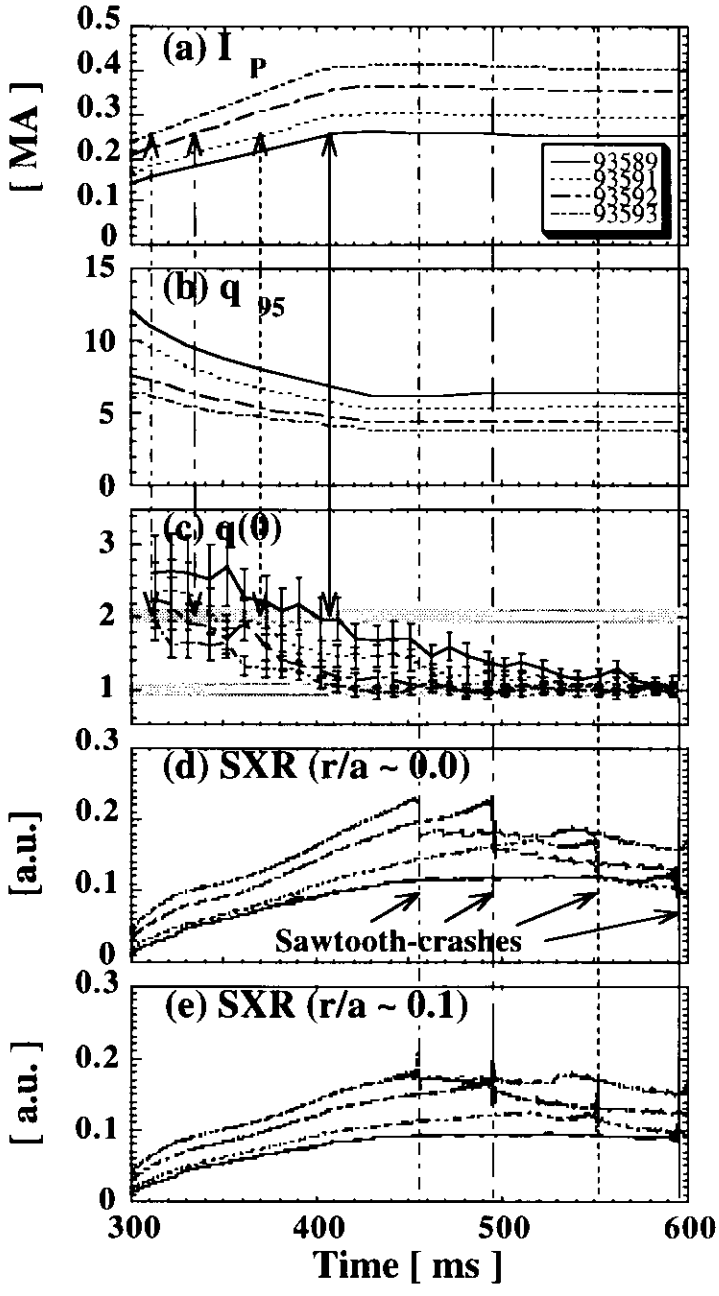

Fig. 4.1.1. Time evolution of L-mode plasmas with various current ramp up rates and sawtooth activities: (a) plasma current, (b) safety factor at r/a ~ 0.95, (c) safety factor at magnetic axis, and (d) soft X-ray emission with the tangent radius of r/a ~ 0.0, (e) soft X-ray emission with the tangent radius of r/a ~ 0.1.

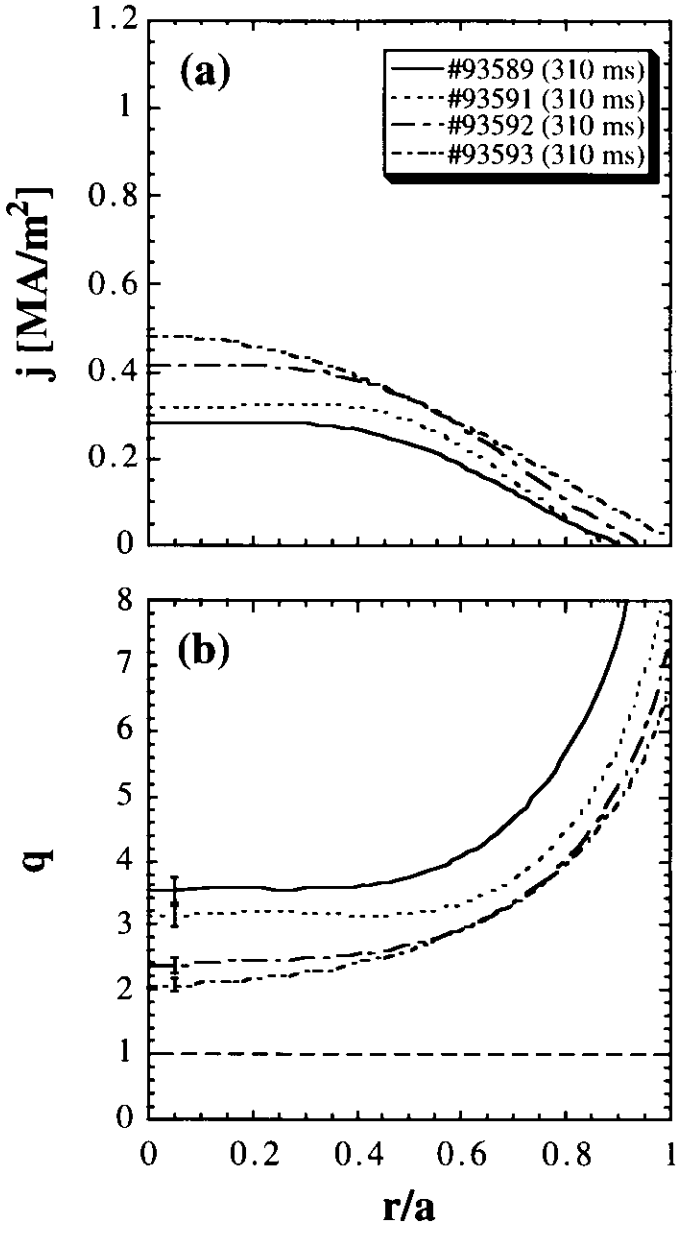

Fig. 4.1.2. The reconstructed profiles of (a) the flux averaged parallel current density and (b) safety factor for discharges shown in Fig. 4.1.1 at 310 ms.

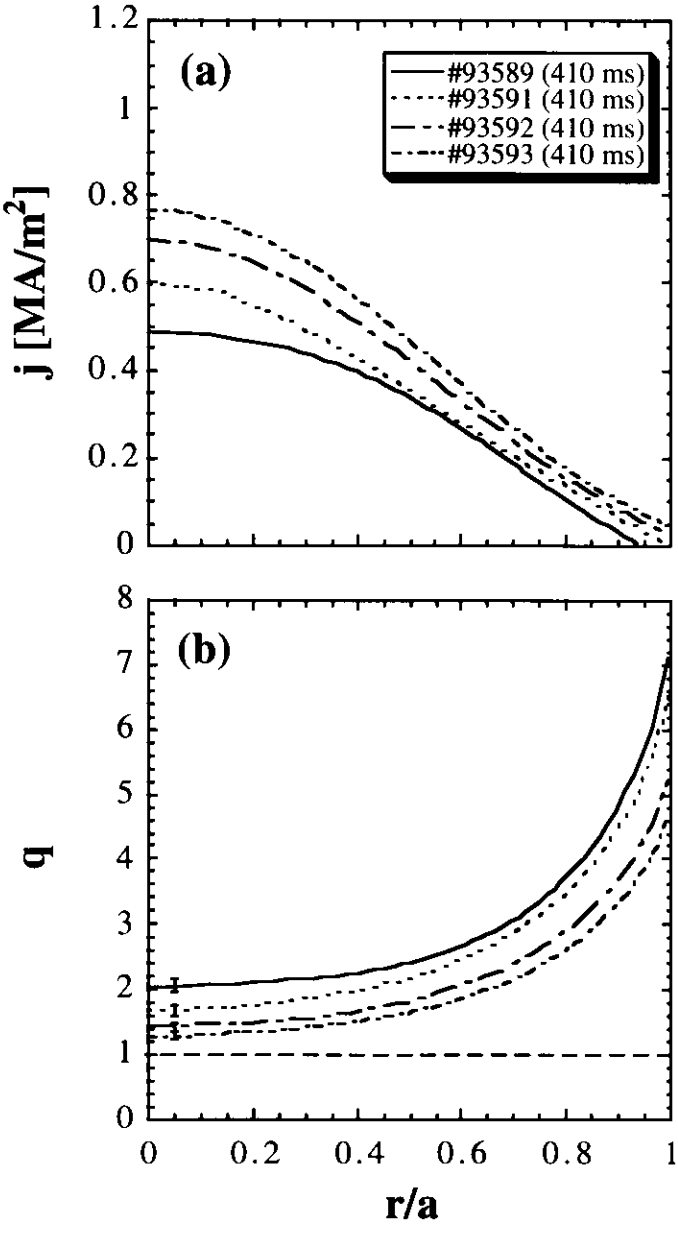

Fig. 4.1.3. The reconstructed profiles of (a) the flux averaged parallel current density and (b) safety factor for discharges shown in Fig. 4.1.1 at 410 ms.

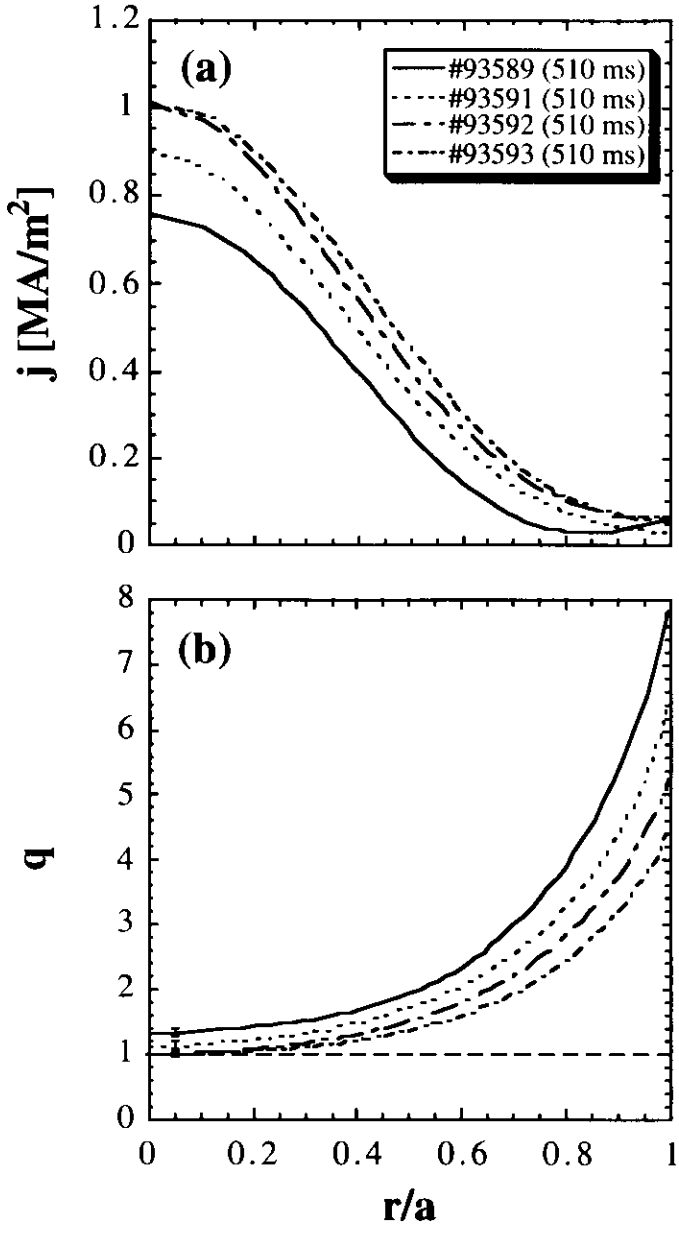

Fig. 4.1.4. The reconstructed profiles of (a) the flux averaged parallel current density and (b) safety factor for discharges shown in Fig. 4.1.1 at 510 ms.

4.2 Comparison with soft X-ray measurements

The soft X-ray emission is produced by the thermal part of the plasma electrons and consists predominantly of the recombination-radiation continuum of the partly ionized oxygen and iron impurities. The radiation intensity is therefore a function of the electron density and temperature and of the impurity concentration. It is thought to reflect the shape and temporal behavior of magnetic flux surfaces occurring MHD activities such as sawtooth collaps (especially, its analysis in terms of two-dimensional contour plots). Comparison between soft X-ray measurements and CUPID results is thus essential to analyze MHD activities qualitatively.

In contrast to discharges with sawteeth collapses discussed in the previous section, though sawtooth crash is usually found within about 5 ms after emerging an m = 1 oscillation in the core region as shown in Fig. 4.2.1, discharges having an m = 1 field deformation and the growth of a related magnetic island without sawtooth collapse are also observed. These series of experiments are done under the condition of a toroidal magnetic field B_T of 2.2 T, a plasma current I_P of 0.25 MA (at flat top) with a limiter configuration and an elongation κ of 1.4. Fig. 4.2.2 shows a comparison of three discharges with different ramp up rate. The balanced NBI with total input power of ~ 0.6 MW is turned on at 300 ms and lasts up to 600 ms. In all discharges, a significant increasing of soft X-ray emission with the tangent radius of r/a ~ 0.0 are observed with oscillations at 100 ~ 150 ms after the plasma current reaches flat top, but sawtooth crash appears nothing yet. As shown in Fig. 4.2.3, these oscillations are localized in the plasma core region and have a frequency of about 1 ~ 10 kHz and a growing amplitude.

The time evolution of CUPID reconstructed j and q-profiles in plasmas shown

in Fig. 4.2.2 are indicated in Fig. 4.2.4 ~ Fig. 4.2.6. Comparing with two-dimensional contour plots of soft X-ray emission and CUPID results, these are consistent quantitatively in term of time evolution toward peaking, but sawtooth crash appears nothing yet showing $q(0) > 1$.

In general, faster current ramp and additional heating during the plasma current ramp using NB and/or RF result in broad or hollow current profile, because these make the current diffusion time longer. The major difference between shots 93584, 93585 and 93586 is the current ramp rates that are 0.4, 0.8 and 1.3 MA/s, especially. Since the timing of NB injection is fixed at 300 ms and lasts up to 600 ms, the slow ramp up discharge (#93584) has the effect of heating during the plasma current ramp, on the other hand, the fast ramp up discharge has its effect nothing. More systematic experiments discriminating the effect of current ramps and NB heating are required.

Returning to Fig. 4.2.1 (c), a rapid increase of internal inductance (l_i), which is reconstructed by EQFIT code, is also observed after controlling I_P constant. It is considered that the penetration of the inductive electric field in a plasma with low electron temperature of about 1 keV is very fast with its time scale of about 100ms. It may cause a significant peaking of central SXR emission with oscillations at earlier time-slice that may be connected with a rotating magnetic island (m=1, n=1) at q = 1 surface. This behavior in the core region is difficult to explain, but very interesting type of MHD activity in tokamaks. Although numerous experimental and theoretical studies have been carried out to date, the sawtooth instability is still not well understood. As shown in Fig. 4.2.1, a sawtooth crash is usually seen within tens of milliseconds after occurrence of this precursor, however, #93586 shows long-lasting oscillation comparing with #93589 (as indicated by solid line in Fig. 4.1.1). Both discharges have nearly same

I_P and dI_P/dt, except for a delay time of 100 ms on balanced NB injection. The difference between shots #93586 and #93589 may come from the condition of the boronized wall by glow discharge cleaning in helium. The former still keep a good condition yet, the latter may be wasted by a repetition of the tokamak discharges as it increases the wall recycling. In fact, the long-lasting oscillations tend to be observed frequently after boronization of the first wall with glow discharge cleaning in helium on JFT-2M. A small enhancement of the impurity accumulation can cause the reduction of the electron temperature and results in the reduction in the local conductivity along the magnetic field lines producing a reduction of current density and a magnetic field perturbation which forms a magnetic island. Although no firm conclusion can be drawn, this is important to understand the mechanism for stabilization of sawteeth completely, as well as the need to control another MHD activity in a future fusion reactor.

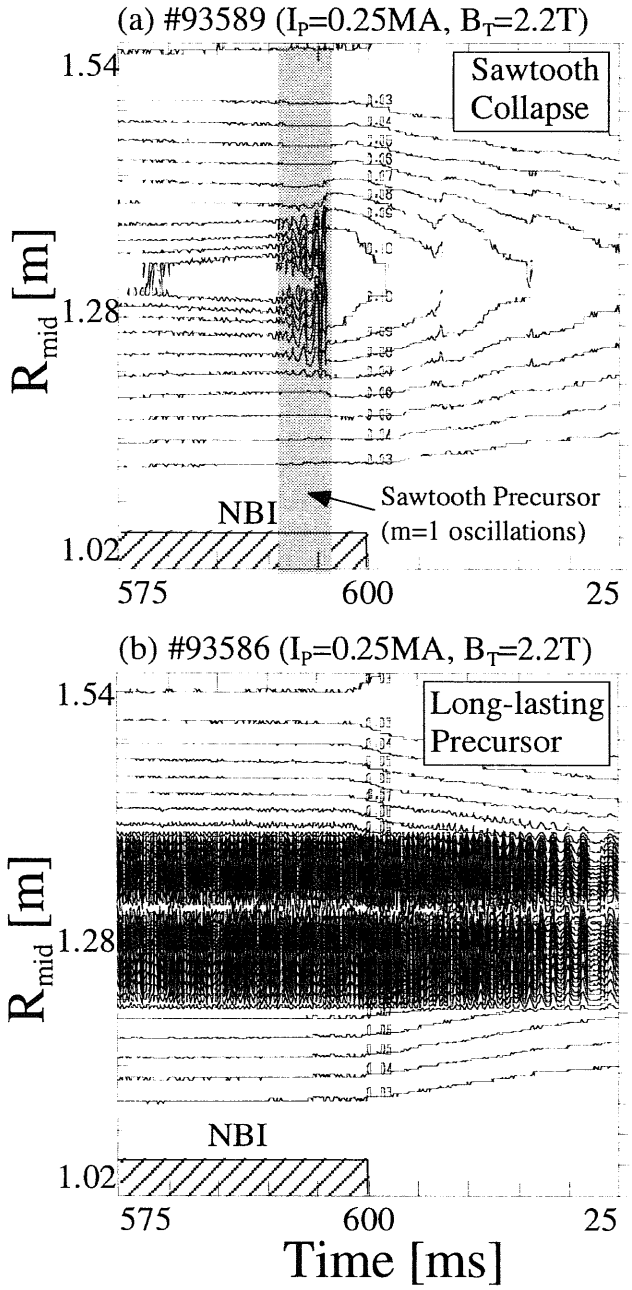

Fig. 4.2.1. Soft X-ray contour plot showing (a) sawtooth crash within about 5 ms after emerging an oscillation in the core region, (b) a long-lasting oscillation.

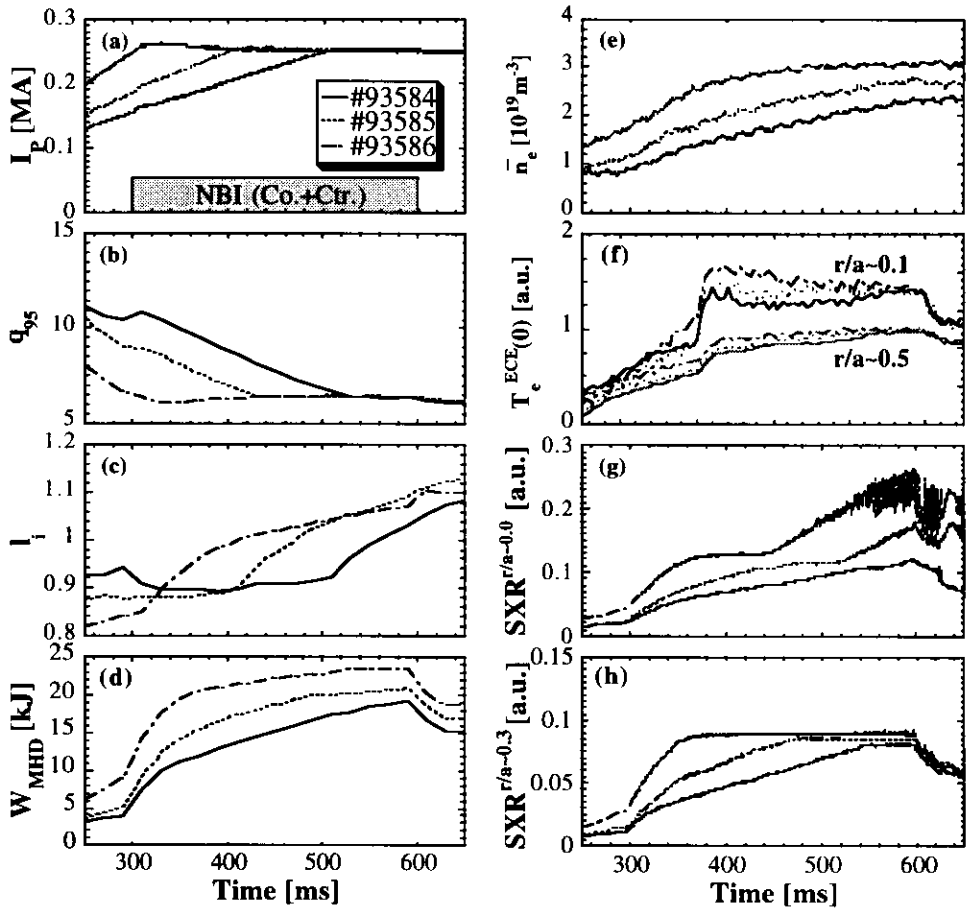

Fig. 4.2.2. Discharge parameters for slow (#93584), intermediate (#93585) and fast (#93586) ramp up. (a) Plasma current and input power of co and ctr-NBI. Reconstructed global parameters of (b) Safety factor at r/a = 0.95, (c) Internal inductance and (d) Stored energy. (e) Line averaged electron density from the chord passing through nearly magnetic axis. (f) Electron temperature measured by ECE at r/a ~ 0.1 and 0.5. (g, f) Soft X-ray emission with the tangent radius of r/a ~ 0.0 and 0.3, especially.

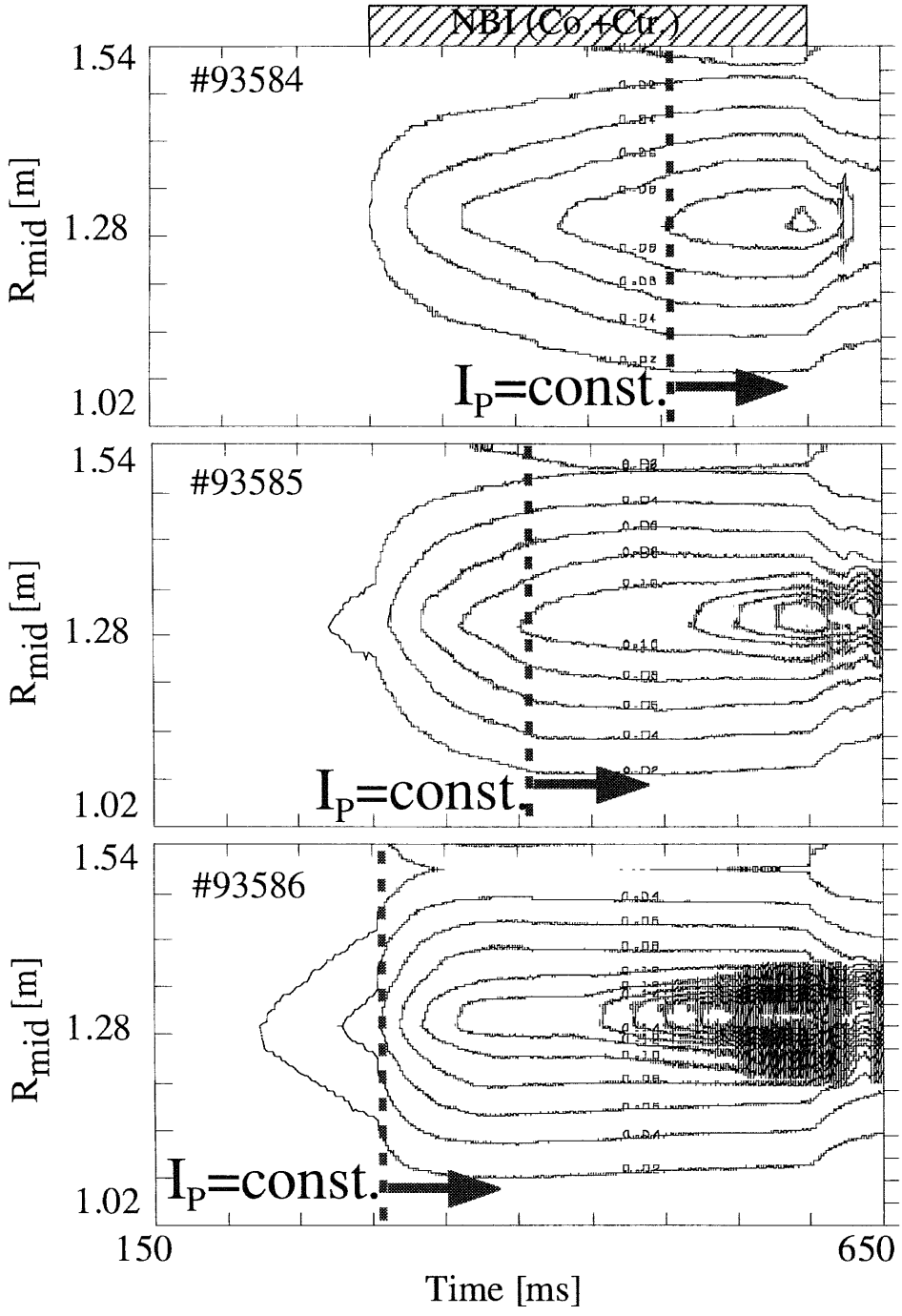

Fig. 4.2.3. Soft X-ray contour plot showing a significant peaking in the plasma core region at 100 ~ 150 ms after the plasma current reaches flat top in all discharges.

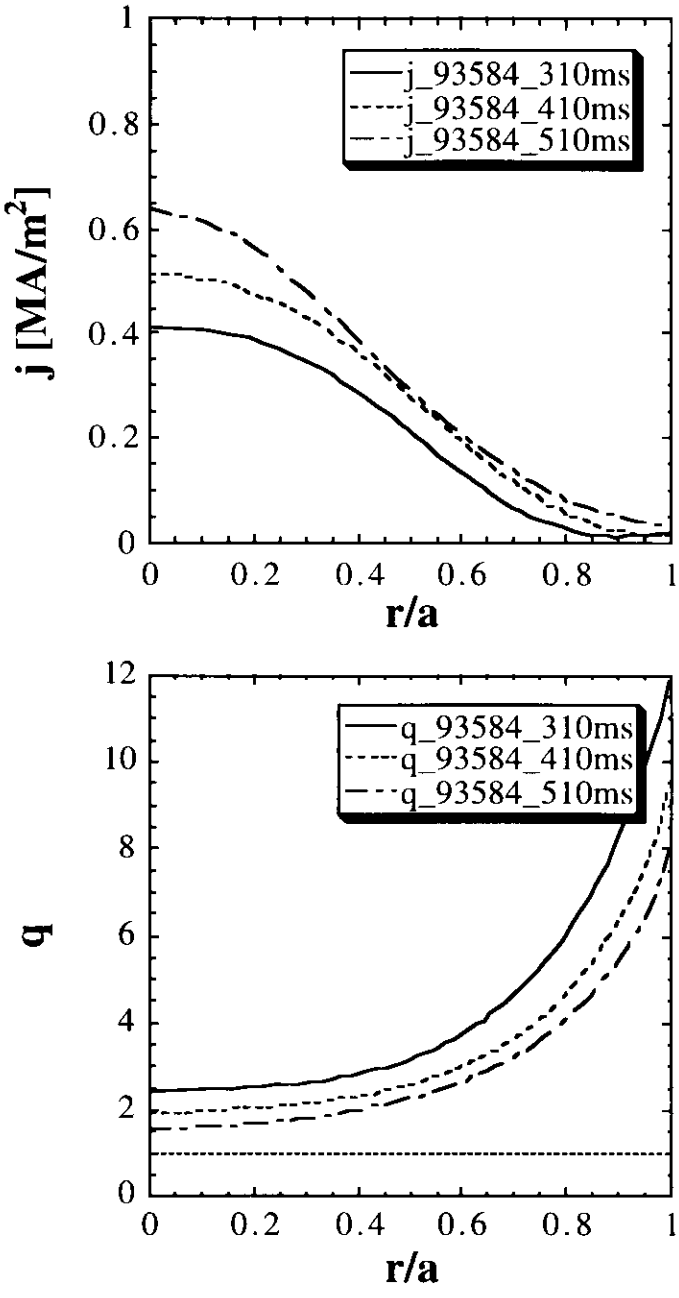

Fig. 4.2.4. The reconstructed profiles of (a) the flux averaged parallel current density and (b) safety factor for #93584 discharge shown in Fig. 4.2.2.

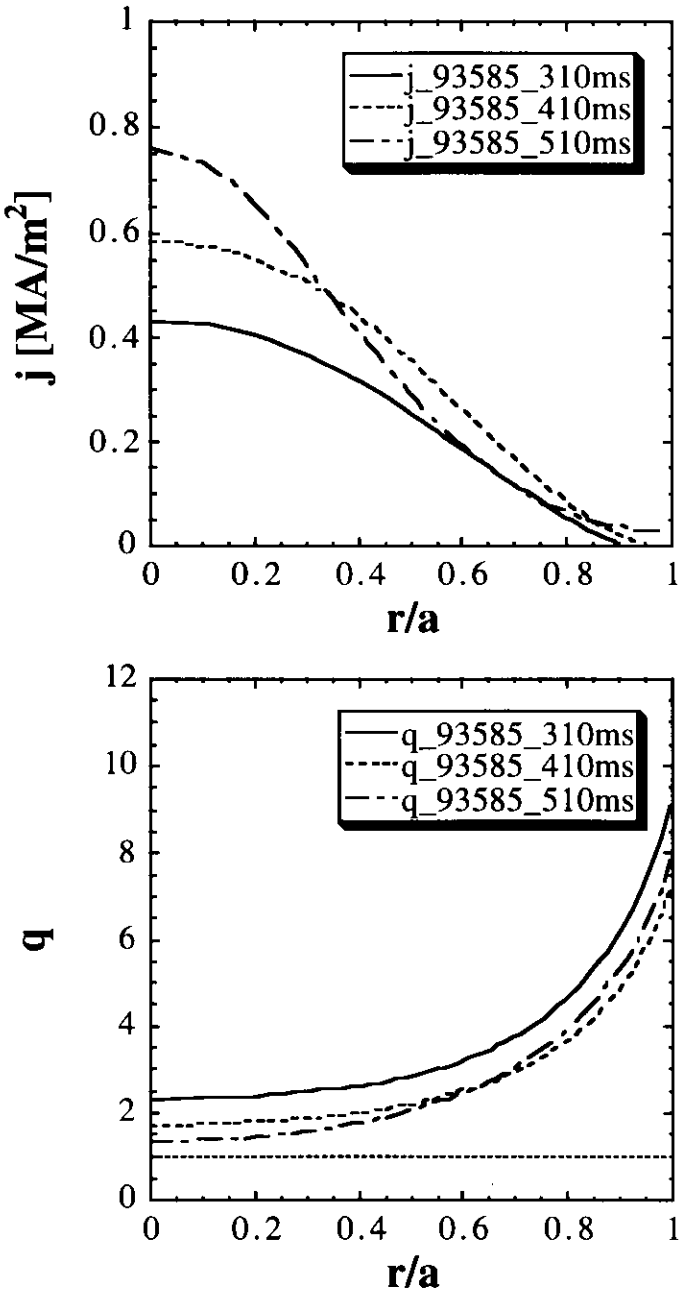

Fig. 4.2.5. The reconstructed profiles of (a) the flux averaged parallel current density and (b) safety factor for #93585 discharge shown in Fig. 4.2.2.

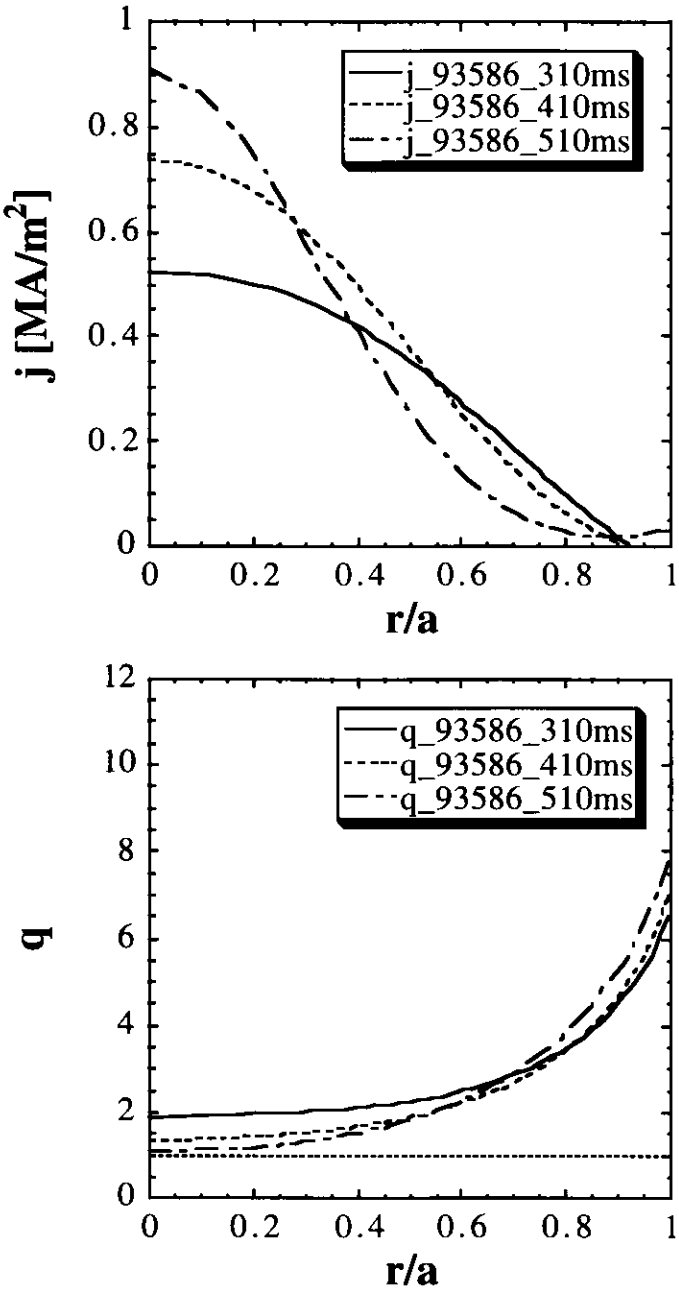

Fig. 4.2.6. The reconstructed profiles of (a) the flux averaged parallel current density and (b) safety factor for #93586 discharge shown in Fig. 4.2.2.

4.3. Radial electric field measurements

Fig. 4.3.1 (a ~ f) show the typical waveforms of two plasmas where NB of opposite direction (solid lines are co-parallel to the plasma current and dashed lines are counter-parallel) are injected with P_{NB} ~ 0.35 MW to identical target plasma with line averaged density of ~ 2.5×10^{19} m^{-3}. These experiments are performed under the condition of the I_P of 0.25 MA and B_T of 2.2 T with a limiter configuration. In the case of co-NBI (shown in solid lines), the multipulsed ctr-NB is injected with P_{NB} ~ 0.25 MW during 20 ms for diagnostic. On the other hand, in the case of ctr-NBI (shown in dashed lines), the multipulsed co-NB is injected with P_{NB} ~ 0.25 MW during 20 ms for diagnostic. As shown in Fig. 4.3.1 (e), viewing co-NB line, it is found that the polarization angle at r/a ~ 0.4 in both co and ctr-NBI cases increase as the timescale of ~ 100 ms after the flat top of I_P (it may be connected with a resistive relaxation of plasma current at these low temperature of ~ 1 keV), however it takes slightly larger value of ~ 0.4 deg. in the case of ctr-NBI (shown in circles with dashed line) compared to the case of co-NBI (shown in solid line) after ~ 100 ms of NB injection. On the other hand, as shown in Fig. 4.3.1 (f), viewing ctr-NB line (the sign of polarization angle is changed due to the change of sign of $\cos(\alpha+\Omega)$ in Eq. 1-2-1), however the polarization angles at r/a ~ 0.4 decrease with similar time scale as viewing co-NB line, it takes rather smaller value of ~ 0.4° in the case of co-NBI after ~ 100 ms of NB injection. The differences in polarization angle of two plasmas after a resistive equilibrium may be directly connected to the effect of E_r formed by the input torque through the radial force balance as show in Eq. 1-3-1. To determine the profile of E_r, the pitch angle profiles assuming E_r = 0 (γ_{p0}: calculated by Eq. 1-2-1 from measured γ_m) are fitted with polynomial curve as

shown Fig. 4.3.2, since the observation points of both co and ctr-NB lines are not quite same. To reduce the statistical uncertainty due to noise, these data are averaged from several shots showing the good repetition as Fig. 4.3.1. Once the profile of γ_{p0} are evaluated from both NB lines that the effect of E_r is near opposite, then the profile of E_r are obtained by simply subtracting it each other and correcting of geometrical constant (α and Ω), v_b and B_T as

$$E_r = v_b B_T \, \delta\{\tan(\gamma_{p0})\} / \delta\{\cos(\Omega) / \cos(\alpha+\Omega)\}, \qquad (4\text{-}3\text{-}1)$$

where $\delta\{\tan(\gamma_{p0})\}$ is the difference of tangent of γ_{p0} and $\delta\{\cos(\Omega) / \cos(\alpha+\Omega)\}$ is the difference of geometrical constant at the same radius.

In this work, the calibration of the offset angle for the pitch angle measurements is performed using the RPM method discussed in section 2.2, where the NB injection is balanced and use Eq. 1-2-3 for the interpretation of the measured polarized signal to the pitch angle assuming $E_r \sim 0$ kV. Although it is a valid assumption at least when these data are used for the equilibrium reconstruction with a systematic uncertainties of about 0.1 ~ 0.2° from the effect of E_r due to the pressure gradient [26], unfortunately, it causes a serious error in the case of E_r measurements. The change in pitch angle is thus only related to the change in the radial electric field due to the change in the toroidal rotation.

Fig. 4.3.3 shows the δE_r (the change in the radial electric field) profiles measured by MSE for both plasmas, also showing the contributions from the terms proportional to the toroidal rotation. It is observed that the negative change in the E_r of about -10 ~ -15 kV is observed at r/a = 0.3 ~ 0.5 in the case of ctr-NBI and the positive change in the E_r of about 5 ~ 10 kV with broad profile is observed in the case of co-NBI. Although the result is in good agreement qualitatively with the relative difference in E_r

of two plasmas estimated from the term proportional to the toroidal rotation, in addition to the statistical uncertainty of about 4 kV/m due to noise, the systematic uncertainty of about factor 2 to this level (4~10 kV/m) due to offset calibration must exist as mentioned above. However its contribution to the measurements of polarization angle is an order of about 0.1°, and it is not cause serious error in reconstruction of q-profile in L-mode plasma considered here. The lack of data of poloidal rotation will also cause the quantitative difference.

Returning to Fig. 4.3.1, line averaged electron density from the chord passing through nearly magnetic axis increases in the case of ctr-NBI and low D_α intensity is observed compared to the co-NBI. It may be connected to the particle confinement improvement due to the formation of negative E_r with ctr-NBI as observed previously [30], although the large sawteeth exist compared with the case of co-NBI. It is limited to half of full power in this work, since the use of additional beam lines which have slightly different injection angle to the midplane cause a large error to the offset angle calibration, and an improvement of energy confinement due to the formation of negative E_r with ctr-NB is not clear. Further study of the improved confinement with ctr-NBI by this MSE system is one of our future subjects.

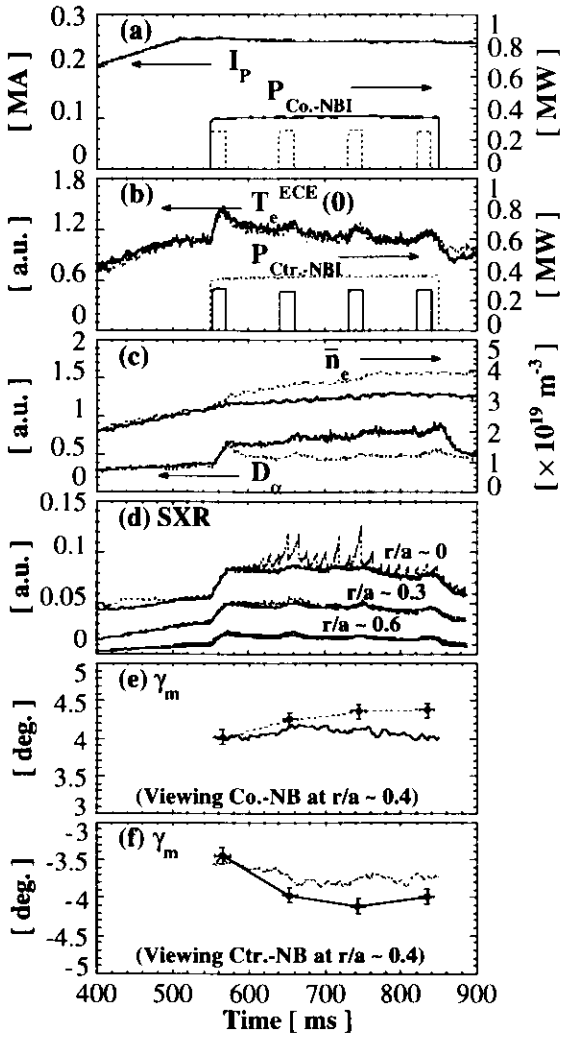

Fig. 4.3.1. Time evolution of two plasmas where NB of opposite direction (solid lines are co-parallel to the plasma current and dashed lines are counter-parallel) are injected with P_{NB} ~ 0.35 MW to identical target plasma: (a) plasma current and input power of co-NBI, (b) central electron temperature measured by ECE and input power of ctr-NBI, (c) line averaged electron density measured by 2mm μ wave interferometer from the chord passing through nearly magnetic axis and D_α emission, (d) soft X-ray emissions with the tangent radius of r/a ~ 0, 0.3, and 0.6, especially, and polarization angle at r/a ~ 0.4 viewing (e) co-NB and (f) ctr-NB, especially.

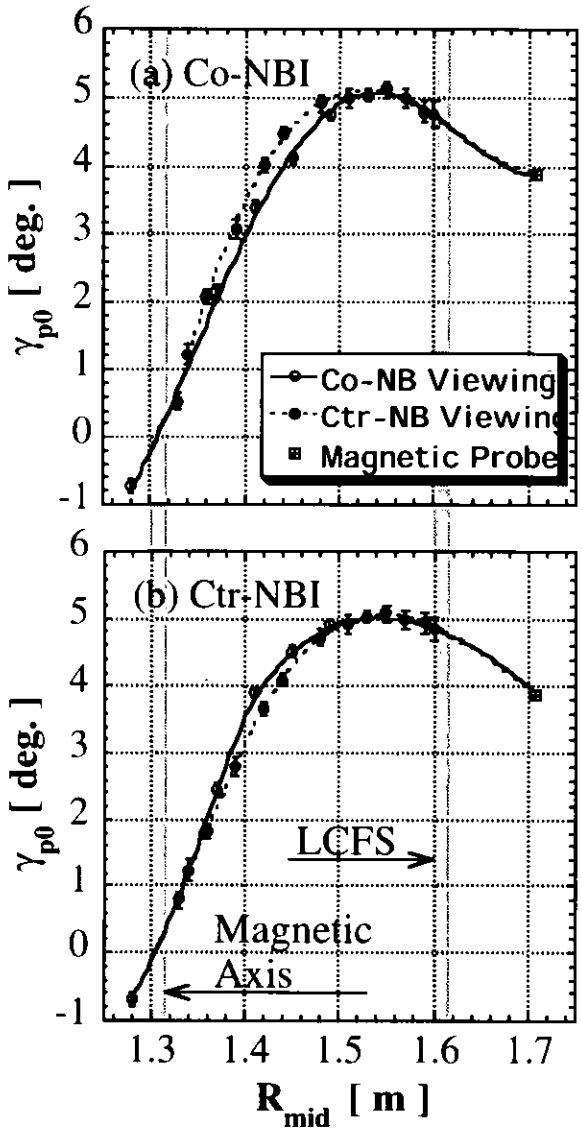

Fig. 4.3.2. The profiles of the pitch angle assuming $E_r = 0$ for the two plasmas of Fig. 4.3.1 at 740 ms: (a) co-NBI and (b) ctr-NBI plasmas. Open circles with solid line are co-NB-viewing chords and closed circles with dashed line are ctr-NB-viewing chords.

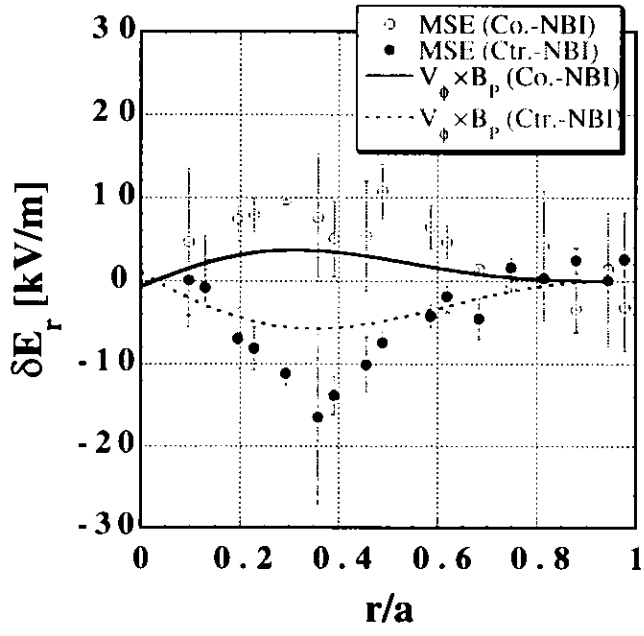

Fig. 4.3.3. The profiles of the δE_r (the change in E_r) measured by MSE for both plasmas. Open circles are in the case of co-NBI and closed circles are in the case of ctr-NBI, also showing the contributions from the terms proportional to the toroidal rotation, for the plasmas with co-NBI (solid line) and ctr-NBI (dashed line).

Chapter 5

Summary

In summary, an 18-channel MSE system has recently been installed on JFT-2M. After the calibration of offset angle by NB injection to the gas filled torus and cross check by RPM method in addition to the calibration of the optics and polarimeter, it is estimated that the uncertainty in the pitch angle measurement is about ~ 0.1 deg. with a time resolution of 10 ms. In L-mode discharges with different I_p and dI_p/dt, it is found that sawtooth crashes emerges reproductively just after the q(0) pass through ~ unity, and it occurs at earlier time-slice as the discharges of larger I_p (and smaller surface q values) at the flat top, irrespective of the dI_p/dt. After sawtooth crash, the q(0) keeps constant value of below ~ unity throughout the sawtooth cycle as observed in many tokamaks. Although the sawtooth oscillations are not readily visible on the MSE with a fixed time resolution of 10 ms due to the relatively high frequency (100 Hz) and small amplitude of the sawtooth in this examples, it will be improved using more faster time resolution of 1 ms in addition to the application of MSE to the plasma with another MHD activities.

In order to determine the equilibrium selfconsistently, the free boundary equilibrium code (CUPID; CUrrent Profile IDentification code) has also been introduced on JFT-2M, which solves the Grad-Shafranov equation using internal magnetic field data measured by MSE in conjunction with external magnetic data measured by magnetic probes, flux loops, and Rogowski coils at several locations outside the plasma. It is confirmed that CUPID reconstructed q-profile is consistent

quantitatively with the soft X-ray measurements, especially in term of the q = 1 radius. As the result of the equilibrium reconstruction by CUPID code, it is confirmed that plasma currents are ramped up with a broad profile (with a monotonic q-profile), irrespective of dI_P/dt. In this work, it is observed a significant peaking of the current profile with the peaking of the soft X-ray emission in the plasma core, but sawtooth crash appears nothing yet showing $q(0) > 1$. A rapid increase of internal inductance is also observed after controlling I_P constant. It is considered that the penetration of the inductive electric field in a plasma with low electron temperature of about 1 keV is very fast with its time scale of about 100ms. It may cause a significant peaking of central SXR emission with oscillations at earlier time-slice that may be connected with a rotating magnetic island (m=1, n=1) at q = 1 surface. This behavior in the core region is difficult to explain, but very interesting type of MHD activity in tokamaks.

Outstanding feature of the MSE system on JFT-2M is that it makes possible to separate the effect of the E_r from the polarization angle measurements with best sensitivity (about 4 kV/m). Preliminary data of δE_r (the change in the radial electric field) profile in L-mode plasmas has been obtained. It is found that the result is in good agreement qualitatively with the relative difference in E_r estimated from CXRS measurements of toroidal rotation. In this work, it is limited to half of full NB power, since the use of additional beam lines which have slightly different injection angle to the midplane cause a large error to the offset angle calibration, and an improvement of energy confinement due to the formation of negative E_r with ctr-NB is not clear. Further study of the improved confinement with ctr-NBI by this MSE system is one of our future subjects.

REFERENCES

[1] F. M. Levinton et al., Phys. Rev. Lett. **75**, 4417 (1995).

[2] E. J. Strait et al., Phys. Rev. Lett. **75**, 4421 (1995).

[3] X. Litaudon et al., Plasma Phys. Control. Fusion **38**, 1603 (1996).

[4] T. Fujita et al., Phys. Rev. Lett. **78**, 2377 (1997) ; 4529 (errata).

[5] G. M. D. Hogeweij et al., Phys. Rev. Lett. **76**, 632 (1996).

[6] B. W. Rice et al., Plasma Phys. Control. Fusion **38**, 869 (1996).

[7] L. L. Lao et al., Nucl. Fusion **30**, 1035 (1990).

[8] S. H. Batha et al., Nucl. Fusion **36**, 1133 (1996).

[9] F. M. Levinton et al., Phys. Rev. Lett. **63**, 2060 (1989).

[10] D. Wroblewski et al., Rev. Sci. Instrum. **61**, 3522 (1990).

[11] F. M. Levinton et al., Rev. Sci. Instrum. **63**, 5157 (1992).

[12] T. Fujita et al., Fusion Eng. Des. **34-35**, 289 (1997).

[13] D. Wroblewski et al., Rev. Sci. Instrum. **63**, 5140 (1992).

[14] B. W. Rice et al., Nucl. Fusion **37**, 517 (1997).

[15] M. C. Zarnstroff et al., Phys. Plasmas **4**, 1097 (1997).

[16] K. H. Burrell, Phys. Plasmas **4**, 1499 (1997).

[17] B. W. Rice et al., Phys. Rev. Lett. **79**, 2694 (1997).

[18] F. M. Levinton et al., Phys. Rev. Lett. **80**, 4887 (1998).

[19] M. Sato et al., Journal of Plasma and Fusion Research, **75**, 741 (1999).

[20] B. W. Rice, Fusion Eng. Des. **34-35**, 135 (1997).

[21] F. M. Levinton et al., Phys. Fluids B **5**, 2554 (1993).

[22] S. von Goeler et al., Phys. Rev. Lett. **33**, 1201 (1974).

[23] B. B. Kadomtsev, Sov. J. Plasma Phys. **1**, 389 (1975).

[24] A. Weller et al., Phys. Rev. Lett. **59**, 2303 (1987).

[25] H. Soltwisch et al., Plasma Phys. Control. Fusion **39**, 341 (1997).

[26] K. Ida et al., Phys. Rev. Lett. **74**, 1990 (1995).

[27] K. C. Shaing, Phys. Fluids **B2**, 2847 (1990).

[28] J. Kim et al., Phys. Rev. Lett. **72**, 2199 (1994).

[29] K. Ida et al., Plasma Phys. Control. Fusion **38**, 1433 (1996).

[30] K. Ida et al., Phys. Rev. Lett. **68**, 182 (1992).